Geophys. J. Int. (1999) **139,** 325–344

Scattering of *S* waves diffracted at the core–mantle boundary: forward modelling

Valérie Emery,[1,2] Valérie Maupin[3,*] and Henri-Claude Nataf[4]

[1] *Institut de Physique du Globe, CNRS-ULP,* 5 *rue René Descartes,* 67084 *Strasbourg Cedex, France*
[2] *Ecole Normale Supérieure, CNRS URA* 1316, *Paris, France*
[3] *Department of Geophysics, Postbox* 1022, *Blindern,* 0315 *Oslo, Norway. E-mail: valerie.maupin@geofysikk.uio.no*
[4] *Laboratoire de Géophysique Interne et de Tectonophysique, Bâtiment IRIGM,* LBP 53, 38041 *Grenoble cedex* 9, *France*

Accepted 1999 June 7. Received 1999 May 31; in original form 1998 October 27

SUMMARY

The lowermost 200–300 km of the Earth's mantle, known as the D″ layer, is an extremely complex and heterogeneous region where transfer processes between the core and the mantle take place. Diffracted *S* waves propagate over large distances and are very sensitive to the velocity structure of this region. Strong variations of amplitudes and waveforms are observed on recordings from networks of broad-band seismic stations. We perform forward modelling of diffracted *S* waves in laterally heterogeneous structures in order to analyse whether or not these observations can be related to lateral inhomogeneities in D″.

We combine the diffraction due to the core and the scattering due to small-scale volumetric heterogeneities (10–100 km) by coupling single scattering (Born approximation) with the Langer approximation, which describes S_{diff} wave propagation. The influence on the direct as well as on the scattered wavefields of the CMB as well as of possible tunnelling in the core or in D″ is fully accounted for. The *SH* and the *SV* components of the diffracted waves are analysed, as well as their coupling.

The modelling is applied in heterogeneous models with different geometries: isolated heterogeneities, vertical cylinders, horizontal inhomogeneities and random media. Amplitudes of scattered waves are weak and only velocity perturbations of the order of 10 per cent over a volume of $240 \times 240 \times 300$ km^3 produce visible effects on seismograms. The two polarizations of S_{diff} have different radial sensitivities, the *SH* components being more sensitive to heterogeneities closer to the CMB. However, we do not observe significant time-shifts between the two components similar to those produced by anisotropy. The long-period S_{diff} have a poor lateral resolution and average the velocity perturbations in their Fresnel zone. Random small-scale heterogeneities with ± 10 per cent velocity contrast in the layer therefore have little effect on S_{diff}, in contrast to their effect on *PKIKP*.

Key words: D″, diffraction, polarization, *S* waves, scattering, synthetic waveforms.

1 INTRODUCTION

The core–mantle boundary (CMB) is a major discontinuity in the Earth with strong contrasts in density, viscosity and chemical composition. The core appears very homogeneous to seismic waves (Souriau & Poupinet 1991), in contrast with the lowermost 200 or 300 km of the mantle, known as the D″ region, where strong lateral heterogeneities are present at small ($\sim$10 km) to large ($\sim$1000 km) scales [for reviews on D″, see Loper & Lay (1995), Weber *et al.* (1996) and Lay *et al.* (1998)]. In particular, precursors of short-period *PKIKP* or *PKKP* waves have been interpreted as scattering by small-scale heterogeneities located in the D″ region (Bataille *et al.* 1990; Haddon & Cleary 1974; Husebye *et al.* 1976) as well as the coda of short-period diffracted *P* waves (Bataille & Lund 1996; Tono & Yomogida 1996, 1997). In the case of precursors, the source of scattering is inferred to be either volumetric inhomogeneities with *P*-velocity fluctuations of several per cent and scale lengths of 10–100 km, or core–mantle topography bounded by 500 m fluctuations (Doornbos 1976, 1978). A more recent analysis seems to indicate that small and weak volumetric heterogeneities ($\sim$8 km, 1 per cent velocity perturbation) may exist throughout the mantle (Hedlin *et al.* 1997).

* Corresponding author.

As they propagate a long distance along the CMB, diffracted waves, mainly P_{diff} and SH_{diff}, have been used to study the velocity structure in the D″ layer (Doornbos & Mondt 1979a; Mula 1981). Large-scale lateral heterogeneities have been found (Hock *et al.* 1997; Souriau & Poupinet 1994; Sylvander *et al.* 1997; Wysession & Okal 1988) with 4 per cent maximum velocity perturbations and strong variations of the Poisson coefficient, favouring chemical anomalies (Wysession *et al.* 1992). A promising procedure for investigating both radial profiles and lateral variations of lower mantle shear velocity is to model simultaneously *SH–SKS* differential traveltimes, amplitude ratios of *SV/SKS* and S_{diff} wave shapes (Ritsema *et al.* 1997). In the Pacific region, SV_{diff} signals exhibit considerable waveform and amplitude variability. Significant small-scale (100–500 km) shear velocity heterogeneity (0.5–1 per cent) is required to explain scatter in the differential times and amplitude ratios. Moreover, observations of time delays between SH_{diff} and SV_{diff} have revived the idea of the possible presence of anisotropy in the D″ layer (Garnero & Lay 1997; Kendall & Silver 1996; Maupin 1994; Ritsema *et al.* 1998; Vinnik *et al.* 1989, 1995, 1998).

In this paper, our scope is to study the effects of lateral heterogenity in D″ on the characteristics of the diffracted *S* waves; in particular, how their waveforms are distorted and their polarizations possibly modified. Following Doornbos & Mondt (1979a) and to avoid confusion in terminology, we will use the word 'scattering' to indicate wave interaction with relatively small-scale irregularities. The word 'diffraction' will be used here in connection with the interaction of the wavefield with a smooth boundary, in this case the CMB. The combination of scattering by small-scale inhomogeneities and diffraction by the core is not easy to study. The diffraction will be modelled using the full wave theory (also called the Langer approximation) developed by Richards (1973, 1976). This approximation is an extension of the high-frequency WKBJ theory. It is accurate in the turning-point region of the ray, which is situated near the CMB interface, and has been used to study *SmKS* waves (Choy 1977), *PKnIKP* waves (Cormier & Richards 1977) and diffracted waves (Doornbos 1981; Doornbos & Mondt 1979a,b; Maupin 1994; Mondt 1977). The main difference with the WKBJ approximation is the frequency dependence of transmission–reflection coefficients. These coefficients incorporate the effects of curvature of the discontinuity and the tunnelling phenomenon at grazing incidence (Richards 1976). In tunnelling, rays that turn just above or below a boundary can interact with the boundary at finite frequency. For rays bottoming just above a boundary, transmitted real rays can be excited below the boundary (Cormier & Richards 1988). Moreover, the Langer approximation is valid if a unique turning point exists for each wave type in a layer. This condition implies that the velocity gradient must satisfy the relation $dv/dz < 0$ or $dv/dr < v/r$ (Doornbos & Mondt 1979a). A satisfactory comparison between the full wave theory and the reflectivity method (Fuchs 1968; Fuchs & Müller 1971) has been made by Choy *et al.* (1980). The scattering is described within the Born approximation. The simplicity of this theory and its implementation have guided our choice: it can be considered as a first step before taking into account more complete theories. In the Born approximation, the incident wave interacts only once with each heterogeneity (first-order scattering), and multiple interactions between heterogeneities are assumed to be negligible. Details about the validity of the Born approximation can be found in Hudson & Heritage (1981). In this study we find that the scattered fields remain small compared to the direct ones. This shows *a posteriori* that the Born approximation should give us reasonably accurate results in the first instance.

In the first part of this paper, we combine the full wave theory with the Born approximation in order to develop an adequate theory to model the scattering of diffracted waves. In the second part, we analyse the characteristics of S_{diff} waves in some simple geophysically relevant situations such as a vertical plume, a localized low-velocity zone and small inhomogeneities distributed in a random way in the D″ layer.

2 THEORY

2.1 Scattering in the Born approximation

Our aim is to model the effects of a point heterogeneity on diffracted *S* waves (Fig. 1). The propagation of S_{diff} waves is treated with the Langer approximation and we only consider single scattering (Born approximation). We focus on the coupling between the two polarizations of *S* waves by volumetric heterogeneities. Indeed, scattered *P* waves have a shorter traveltime than S_{diff} waves. These scattered *P* waves cannot interfere with the primary S_{diff} wave.

The general equation of motion in a spherical earth can be written as

$$\rho \ddot{u}_i = f_i + \sigma_{ij,j}\,, \tag{1}$$

where **u** is the displacement vector, $\boldsymbol{\sigma}$ the stress tensor and **f** the source force vector. For an isotropic medium, the stress and strain tensors are related by

$$\sigma_{ij} = \lambda \delta_{ij} e_{kk} + 2\mu e_{ij}\,, \tag{2}$$

where

$$e_{ij} = \frac{1}{2}\left(\frac{\partial u_i}{\partial x_j} + \frac{\partial u_j}{\partial x_i}\right) \tag{3}$$

is the strain tensor. The effect of lateral heterogeneity is treated in a linearized way by using the Born approximation

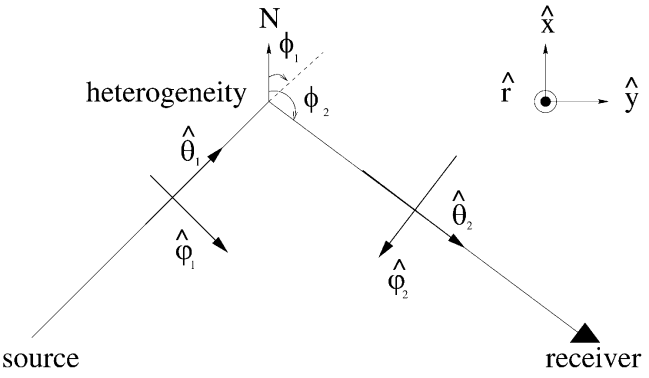

Figure 1. Coordinate systems used in this study. In ($\hat{\boldsymbol{r}}$, $\hat{\boldsymbol{x}}$, $\hat{\boldsymbol{y}}$), *r* corresponds to the radius, *x* to north and *y* to east.

for the scattered wave. Suppose that the structural parameters in the medium can be written in the following way:

$$\begin{aligned}\mu(\mathbf{r}) &= \mu(r,\,\theta,\,\phi) = \mu^0(r) + \Delta\mu(r,\,\theta,\,\phi)\,,\\ \lambda(\mathbf{r}) &= \lambda(r,\,\theta,\,\phi) = \lambda^0(r) + \Delta\lambda(r,\,\theta,\,\phi)\,,\\ \rho(\mathbf{r}) &= \rho(r,\,\theta,\,\phi) = \rho^0(r) + \Delta\rho(r,\,\theta,\,\phi)\,.\end{aligned} \tag{4}$$

The parameters μ^0, λ^0 and ρ^0 define a laterally homogeneous background medium. All calculations are performed in the frequency domain. Combining eqs (1), (2) and (4), the equation of motion of the laterally heterogeneous system can be written as

$$L_{ij}u_j = f_i\,, \quad \text{with} \quad L_{ij} = -\delta_{ij}\rho\omega^2 - \partial_i\lambda\partial_j - \partial_j\mu\partial_i - \delta_{ij}\partial_k\mu\partial_k \tag{5}$$

(Snieder 1986a). The operator can be developed as $\mathbf{L} = \mathbf{L}^0 + \mathbf{\Delta L}$ and the displacement field $\mathbf{u} = \mathbf{u}^0 + \mathbf{\Delta u}$. If these expressions are inserted in eq. (5), the terms of zeroth order and first order in perturbation lead to the relations

$$\mathbf{L}^0\mathbf{u}^0 = \mathbf{f}\,, \tag{6}$$

$$\mathbf{L}^0\mathbf{\Delta u} = -\mathbf{\Delta L u}^0\,. \tag{7}$$

Eqs (6) and (7) can both be solved with the Green's function $\mathbf{G}$ of the background medium. This leads to the following expressions for the direct wave:

$$\mathbf{u}^{\mathrm{dir}} = \mathbf{u}^0 = \mathbf{Gf}\,, \tag{8}$$

and for the scattered wave:

$$\mathbf{u}^{\mathrm{scat}} = \mathbf{\Delta u} = -\mathbf{G\Delta L u}^{\mathrm{dir}} = -\mathbf{G\Delta LGf}\,. \tag{9}$$

The previous equations are an abbreviated notation for

$$u_i^{\mathrm{dir}}(\mathbf{r},\,\omega) = G_{ij}F_j = \int dV_{\mathrm{s}}G_{ij}(\mathbf{r},\,\mathbf{r}_{\mathrm{s}},\,\omega)f_j(\mathbf{r}_{\mathrm{s}},\,\omega)\,, \tag{10}$$

$$u_i^{\mathrm{scat}}(\mathbf{r},\,\omega) = -\int dV_{\mathrm{h}} \int dV_{\mathrm{s}}G_{ij}(\mathbf{r},\,\mathbf{r}_{\mathrm{h}})\Delta L_{jk}(\mathbf{r}_{\mathrm{h}})G_{kl}(\mathbf{r}_{\mathrm{h}},\,\mathbf{r}_{\mathrm{s}})f_l(\mathbf{r}_{\mathrm{s}},\,\omega)\,, \tag{11}$$

where V_{s} is the source volume and V_{h} the volume of the inhomogeneity. The operator representing the heterogeneity is

$$\begin{aligned}\Delta L_{jk}(\mathbf{r}_{\mathrm{h}}) = &-\delta_{jk}\Delta\rho(\mathbf{r}_{\mathrm{h}})\omega^2 - \partial_j^{\mathrm{h}}\Delta\lambda(\mathbf{r}_{\mathrm{h}})\partial_k^{\mathrm{h}}\\ &-\partial_k^{\mathrm{h}}\Delta\mu(\mathbf{r}_{\mathrm{h}})\partial_j^{\mathrm{h}} - \delta_{jk}\partial_l^{\mathrm{h}}\Delta\mu(\mathbf{r}_{\mathrm{h}})\partial_l^{\mathrm{h}}\,.\end{aligned} \tag{12}$$

The differentiations ∂^{h} are all with respect to the $\mathbf{r}_{\mathrm{h}}$ coordinates of the heterogeneity. Note that the differentiations apply both to the Green's function on the right of $\mathbf{\Delta L}$ and to the lateral heterogeneities $\Delta\lambda(\mathbf{r}_{\mathrm{h}})$ and $\Delta\mu(\mathbf{r}_{\mathrm{h}})$. The differentiation over these last quantities can be removed by partial integration (e.g. Snieder 1986a). For example, the $\Delta\lambda(\mathbf{r}_{\mathrm{h}})$ term can be rewritten as follows:

$$\begin{aligned}&\int dV_{\mathrm{h}}G_{ij}(\mathbf{r},\,\mathbf{r}_{\mathrm{h}})\partial_j^{\mathrm{h}}[\Delta\lambda(\mathbf{r}_{\mathrm{h}})\partial_k^{\mathrm{h}}G_{kl}(\mathbf{r}_{\mathrm{h}},\,\mathbf{r}_{\mathrm{s}})]f_l\\ &\quad= -\int dV_{\mathrm{h}}[\partial_j^{\mathrm{h}}G_{ij}(\mathbf{r},\,\mathbf{r}_{\mathrm{h}})]\Delta\lambda(\mathbf{r}_{\mathrm{h}})[\partial_k^{\mathrm{h}}G_{kl}(\mathbf{r}_{\mathrm{h}},\,\mathbf{r}_{\mathrm{s}})]f_l\\ &\qquad+\int dS_{\mathrm{h}}G_{ij}(\mathbf{r},\,\mathbf{r}_{\mathrm{h}})]\Delta\lambda(\mathbf{r}_{\mathrm{h}})[\partial_k^{\mathrm{h}}G_{kl}(\mathbf{r}_{\mathrm{h}},\,\mathbf{r}_{\mathrm{s}})]f_l\,.\end{aligned} \tag{13}$$

The partial integration yields a surface integral, which is zero for buried scatterers as in our case (Snieder 1986a) [for a more general justification, see Snieder (1986b) or Tarantola (1987)]. We suppose that the heterogeneity is localized in a region V_{h} with characteristic lengths small compared to the wavelength (Rayleigh scattering). In this case, we can consider the Green's function to be constant over the volume V_{h}. Doing the same partial integration for the $\Delta\mu(\mathbf{r}_{\mathrm{h}})$ terms, we finally obtain

$$\begin{aligned}u_i^{\mathrm{scat}}(\mathbf{r},\,\omega) = [&\Delta\rho\omega^2 V_{\mathrm{h}}G_{ij}(\mathbf{r},\,\mathbf{r}_{\mathrm{h}})G_{jl}(\mathbf{r}_{\mathrm{h}},\,\mathbf{r}_{\mathrm{s}})\\ &-\Delta\lambda V_{\mathrm{h}}(\partial_j^{\mathrm{h}}G_{ij}(\mathbf{r},\,\mathbf{r}_{\mathrm{h}}))\,(\partial_k^{\mathrm{h}}G_{kl}(\mathbf{r}_{\mathrm{h}},\,\mathbf{r}_{\mathrm{s}}))\\ &-\Delta\mu V_{\mathrm{h}}(\partial_k^{\mathrm{h}}G_{ij}(\mathbf{r},\,\mathbf{r}_{\mathrm{h}}))\,(\partial_j^{\mathrm{h}}G_{kl}(\mathbf{r}_{\mathrm{h}},\,\mathbf{r}_{\mathrm{s}}))\\ &-\Delta\mu V_{\mathrm{h}}(\partial_k^{\mathrm{h}}G_{ij}(\mathbf{r},\,\mathbf{r}_{\mathrm{h}}))\,(\partial_k^{\mathrm{h}}G_{jl}(\mathbf{r}_{\mathrm{h}},\,\mathbf{r}_{\mathrm{s}}))]f_l(\mathbf{r}_{\mathrm{s}},\,\omega)\,,\end{aligned} \tag{14}$$

which we can write in a more compact form with an operator $\mathbf{\Delta M}$,

$$u_i^{\mathrm{scat}}(\mathbf{r},\,\omega) = G_{ij}(\mathbf{r},\,\mathbf{r}_{\mathrm{h}})\Delta M_{jk}(\mathbf{r}_{\mathrm{h}})G_{kl}(\mathbf{r}_{\mathrm{h}},\,\mathbf{r}_{\mathrm{s}})f_l(\mathbf{r}_{\mathrm{s}},\,\omega)\,, \tag{15}$$

or, in a matricial form,

$$\mathbf{u}^{\mathrm{scat}}(\mathbf{r},\,\omega) = \mathbf{G}(\mathbf{r},\,\mathbf{r}_{\mathrm{h}})\mathbf{\Delta M}(\mathbf{r}_{\mathrm{h}})\mathbf{G}(\mathbf{r}_{\mathrm{h}},\,\mathbf{r}_{\mathrm{s}})\mathbf{f}(\mathbf{r}_{\mathrm{s}},\,\omega)\,, \tag{16}$$

where the derivatives in the operator $\mathbf{\Delta M}$ act only on Green's functions. This is a completely general expression for the scattered field in the Rayleigh–Born approximation (Snieder 1986a). We now have to introduce in this expression a Green's function that is appropriate for representing the diffracted *S* waves.

2.2 Green's function for diffracted *S* waves in a laterally homogeneous medium

In the following, we calculate the Green's functions needed in eq. (16). Diffracted waves cannot be modelled by ray theory. Within D″, the S_{diff} waves are close to their turning point. At the frequencies we are interested in, the most appropriate method to model them is the Langer approximation, which is an extension of the WKBJ approximation for waves close to their turning point (Richards 1973, 1976). The S_{diff} waves are the poles of the reflection coefficients at the CMB. We need, therefore, to account for the interaction of the direct and scattered wavefield with the CMB. This will be achieved by inserting the boundary conditions on D″ in the Green's functions using a reflectivity-like scheme (Kennett 1983). Although it is used here primarily to account for the CMB, we note that this procedure models properly the whole propagation process within D″, even for complicated models of D″. In a model with a discontinuity at the top of the D″ layer, for example, it would handle the interaction of the wavefield with that discontinuity as well as multiple reflections within D″. In the lower mantle above D″, the wavefield is assumed to be a simple downgoing incident wave and two upgoing waves, the direct and scattered waves. The WKBJ approximation will be used to describe the wavefield in this part of the model (Fig. 2). We assume that the inhomogeneity is situated exclusively in the D″ layer.

We will first recall some elements concerning the Langer approximation. We will then combine them with the boundary conditions and source terms to express the Green's functions.

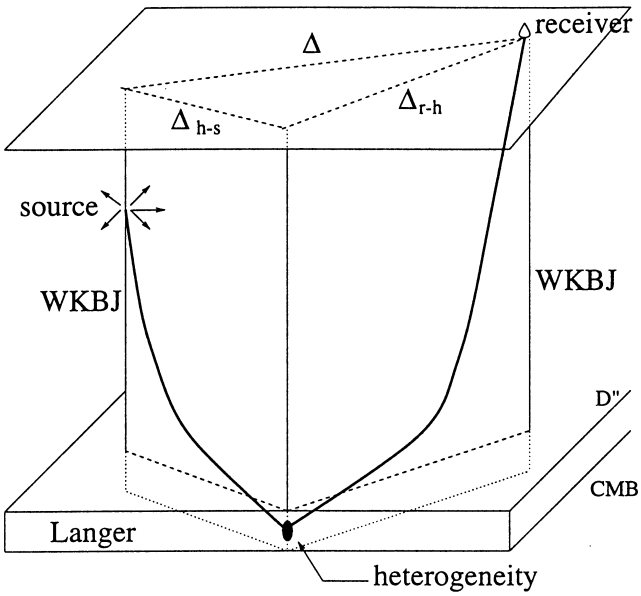

Figure 2. Use of the Langer approximation in the D″ layer and of the WKBJ approximation in the rest of the mantle to calculate the wavefield.

2.2.1 *The Langer approximation*

In spherical coordinates, displacement, radial stresses and source terms may be expanded in terms of spherical harmonics (Chapman & Orcutt 1985). In the high-frequency approximation (equivalent to large l, small m and the receiver away from the poles), the spherical harmonic vectors align with the unit vectors of the coordinate system and the expansion may be reduced to

$$\begin{pmatrix} \mathbf{u} \\ \boldsymbol{\tau}/\omega \end{pmatrix} = \sum_l \sum_m \mathbf{B}_l^m Y_l^m(\theta, \phi)\,. \tag{17}$$

Keeping only the terms that represent the waves moving away from the source, the asymptotic form for Y_l^m is

$$Y_l^m(\theta, \phi) = (i)^m Y_l(\theta) \exp(im\phi)\,, \tag{18}$$

with

$$Y_l(\theta) = \sqrt{\frac{2l+1}{4\pi}}\, Q_l^{(2)}(\cos\theta) \tag{19}$$

and

$$Q_l^{(2)}(\cos\theta) = \frac{\exp\left[i\left(l+\frac{1}{2}\right)\theta - i\,\frac{\pi}{4}\right]}{\sqrt{2\pi l \sin\theta}}\,. \tag{20}$$

In the case of a point force at the pole,

$$\mathbf{f}(r, \theta, \phi) = \mathbf{F}\,\frac{\delta(r-r_s)}{r^2} \lim_{\theta_s \to 0} \delta(\theta-\theta_s)\delta(\phi)\,, \tag{21}$$

the expansion of the source terms becomes, in the same conventions as in eq. (17),

$$\begin{aligned} \mathbf{F}_l^{mT} &= (H_l^m \quad I_l^m \quad J_l^m) \\ &= \frac{\delta(r-r_s)}{r^2} \lim_{\theta_s \to 0} \mathbf{F}^T \cdot (\mathbf{R}_l^{m*}(\theta_s, 0) \;\; i\mathbf{S}_l^{m*}(\theta_s, 0) \;\; -i\mathbf{T}_l^{m*}(\theta_s, 0))\,, \end{aligned} \tag{22}$$

where $\mathbf{R}_l^m$, $\mathbf{S}_l^m$ and $\mathbf{T}_l^m$ are the spherical harmonic vectors. The expansion has non-zero values only for $m = 0, +1$ and -1:

$$H_l^0 = \frac{\delta(r-r_s)}{r^2}\sqrt{\frac{2l+1}{4\pi}}\,F_r\,,$$

$$I_l^m = \frac{\delta(r-r_s)}{r^2}\sqrt{\frac{2l+1}{4\pi}}\,\frac{1}{2}\,(\mp iF_\theta - F_\phi)\,, \qquad m = \pm 1\,, \tag{23}$$

$$J_l^m = \frac{\delta(r-r_s)}{r^2}\sqrt{\frac{2l+1}{4\pi}}\,\frac{1}{2}\,(F_\theta \mp iF_\phi)\,, \qquad m = \pm 1\,.$$

Combining eqs (1), (2) and (3), we express the equation of motion for a perfectly elastic, isotropic and spherically symmetric medium. The spherical harmonics decomposition is such that this equation reduces to an equation in the radial coordinate only:

$$\frac{d\mathbf{B}_l^m}{dr} = \omega \mathbf{A} \mathbf{B}_l^m + \begin{pmatrix} 0 \\ -\mathbf{F}_l^m/\omega \end{pmatrix}. \tag{24}$$

$\mathbf{A}$ is a 6×6 matrix related to the properties of the medium, independent of the angular frequency ω and of the index m (given in Chapter 9.5 of Aki & Richards 1980a). Since $\mathbf{A}$ is independent of m, the solutions of the differential equation (24) are independent of m, except for the forcing terms. Using eq. (18), eq. (17) can be transformed into

$$\begin{pmatrix} \mathbf{u} \\ \boldsymbol{\tau}/\omega \end{pmatrix} = \sum_l \mathbf{b}_l Y_l(\theta)\,, \tag{25}$$

with

$$\mathbf{b}_l = \sum_m (i)^m \mathbf{B}_l^m \exp(im\phi)\,. \tag{26}$$

Inserting this expression into eq. (24) and using the expression (23) for the expansion of the source term, one can show that $\mathbf{b}_l$ satisfies the differential equation

$$\frac{d\mathbf{b}_l}{dr} = \omega A \mathbf{b}_l + \begin{pmatrix} 0 \\ 0 \\ 0 \\ -F_r \\ -F_\theta \cos\phi - F_\phi \sin\phi \\ F_\theta \sin\phi - F_\phi \cos\phi \end{pmatrix} \frac{1}{\omega r^2}\sqrt{\frac{2l+1}{4\pi}}\,\delta(r-r_s)\,. \tag{27}$$

In the epicentral direction $\phi = 0$, this equation reduces to

$$\frac{d\mathbf{b}_l}{dr} = \omega A \mathbf{b}_l + \begin{pmatrix} 0 \\ -\mathbf{F}/\omega r^2 \end{pmatrix} \sqrt{\frac{2l+1}{4\pi}}\,\delta(r-r_s)\,. \tag{28}$$

In the following, $(l+1/2)$ will be replaced by $k = \omega p$, where k is the horizontal wavenumber and p the horizontal ray parameter, and the index l on $\mathbf{b}$ will be omitted. A solution of eq. (28) can be obtained by transforming the displacement–stress vector $\mathbf{b}$ to the amplitudes $\mathbf{a}$ of down- and upgoing elementary waves, which leads, in the absence of a source, to

$$\mathbf{b} = \mathbf{D}\boldsymbol{\Lambda}\mathbf{a}\,. \tag{29}$$

The columns of the **D** matrix are formed with the eigenvectors of the **A** matrix and correspond to displacement–stress vectors of elementary down- and upgoing *P*, *SV* and *SH* waves (or a combination of down- and upgoing waves below the turning point). **Λ** is a diagonal matrix whose elements are vertical wave functions. As far as possible, we have used the same conventions and normalizations as Cormier & Richards (1988) for the notation in these matrices. In the Langer approximation, *P* and *S* waves travel independently except at layer boundaries, leading to constant amplitudes in each layer.

The goal of this study is to analyse the effect of lateral heterogeneities on the waveforms of *S*-diffracted waves. In the framework of the Born approximation, multiple scattering such as *SPS* scattering cannot be studied. Scattered waves involving one conversion from *S* to *P* or from *P* to *S* have traveltimes quite different from those of the pure *S* phases, and will not interfere with the direct *S* wave. We can therefore restrict our analysis to *SS* scattering. In the models we are using, the *S*-diffracted waves depend on the *P*-wave velocity only through the *P*-wave velocity dependence of the reflection coefficients at the CMB. Except when calculating this reflection coefficient, we can therefore reduce the dimensions of the amplitude vectors **a** and of the **D** and **Λ** matrices, working only with their elements related to the *S* waves. Not doing so would introduce undesirable numerical noise in the calculations. In situations where *P* waves would be of some importance, for example in the presence of an ultra-low-velocity zone, or in order to study $SP_{\rm diff}KS$ waves, the derivation can be performed with the full **a**, **D** and **Λ** matrices. In models with discontinuities at the top of or inside D″, the full **D** and **Λ** matrices can easily be introduced in the calculation of the propagators at the level of the discontinuities, in order to account for the *P*-wave velocity dependence of the reflection and transmission coefficients.

We also define two matrices $\mathbf{\Lambda}^{-1}$ and $\mathbf{D}^{-1}$ that are not exactly the inverses of **Λ** and **D**, but are such that $\mathbf{\Lambda}^{-1}\mathbf{D}^{-1}$ is the inverse of **DΛ**. In the following, we only need the part of the matrices related to *S* waves:

$$\mathbf{\Lambda}=\begin{bmatrix}\grave{\sigma} & & & \\ & \acute{\sigma} & & \\ & & \acute{\sigma} & \\ & & & \grave{\sigma}\end{bmatrix};\quad \mathbf{\Lambda}^{-1}=\frac{-i\omega^2 r^2}{2\rho_s\beta_s^3}\begin{bmatrix}\acute{\sigma} & & & \\ & \grave{\sigma} & & \\ & & \grave{\sigma} & \\ & & & \acute{\sigma}\end{bmatrix}, \tag{30}$$

where ρ_s and β_s are the density and the *S* velocity at the source. In the Langer approximation, the vertical wave functions are expressed in terms of Airy functions:

$$\begin{bmatrix}\grave{\sigma}\\ \acute{\sigma}\end{bmatrix}=\left(\frac{\rho_s}{\rho}\right)^{1/2}\frac{\beta_s^{3/2}}{\beta}\,\frac{2}{\omega r}\left(\frac{\pi}{\chi}\right)^{1/2}\zeta^{1/4}\begin{bmatrix}Ai(-\mathrm{e}^{-2i\pi/3}\zeta)\,\mathrm{e}^{+i\pi/3}\\ Ai(-\mathrm{e}^{+2i\pi/3}\zeta)\,\mathrm{e}^{-i\pi/3}\end{bmatrix}, \tag{31}$$

with

$$\zeta=\frac{3}{2}\,\omega\tau;\quad \tau=\int_{r_{pb}}^{r}\chi dr;\quad \chi=\left[\frac{1}{\beta^2}-\frac{p^2}{r^2}\right]^{1/2}. \tag{32}$$

Below the turning point of the wave, the descending wave $\grave{\sigma}$ is replaced by a stationary wave $\breve{\sigma}=\grave{\sigma}+\acute{\sigma}$ (Cormier & Richards 1977) in order to take into account multiple reflections (Doornbos 1981). At the level of the turning point, the wave function tends to a non-zero limit (Langer 1949). The generalized vertical slownesses are defined as

$$\acute{\eta}=\frac{1}{i\omega\acute{\sigma}}\,\frac{d\acute{\sigma}}{dr};\quad \grave{\eta}=-\frac{1}{i\omega\grave{\sigma}}\,\frac{d\grave{\sigma}}{dr}. \tag{33}$$

In the WKBJ approximation, the Airy functions reduce to exponentials:

$$\begin{bmatrix}\grave{\sigma}\\ \acute{\sigma}\end{bmatrix}=\left(\frac{\rho_s}{\rho}\right)^{1/2}\frac{\beta_s^{3/2}}{\beta}\,\frac{1}{\omega r}\,\frac{1}{\chi^{1/2}}\begin{bmatrix}\mathrm{e}^{-i\omega\tau}\,\mathrm{e}^{+i\pi/4}\\ \mathrm{e}^{+i\omega\tau}\,\mathrm{e}^{-i\pi/4}\end{bmatrix}. \tag{34}$$

The generalized vertical slownesses become, above the turning point, $\grave{\eta}\sim\acute{\eta}\sim\chi$, and below the turning point, $\grave{\eta}\sim-\acute{\eta}\sim-i(p^2/r^2-1/\beta^2)^{1/2}$.

The **D** matrix, built in a convention that is convenient for calculating reflection and transmission coefficients, with the first two columns for downgoing $SV^{\downarrow}$ and $SH^{\downarrow}$ waves and the last two for upgoing waves $SV^{\uparrow}$ and $SH^{\uparrow}$, can be written

$$\mathbf{D}=\begin{bmatrix}\beta p/r & 0 & \beta p/r & 0\\ \beta\grave{\eta} & 0 & -\beta\acute{\eta} & 0\\ 0 & 1 & 0 & 1\\ -2i\rho\beta b\grave{\eta} & 0 & 2i\rho\beta b\acute{\eta} & 0\\ -i\rho\beta a & 0 & -i\rho\beta a & 0\\ 0 & -i\rho\beta^2\grave{\eta} & 0 & -i\rho\beta^2\acute{\eta}\end{bmatrix}, \tag{35}$$

$$\mathbf{D}^{-1}=\begin{bmatrix}2i\rho\beta b\acute{\eta} & i\rho\beta a & 0 & -\beta p/r & -\beta\acute{\eta} & 0\\ 0 & 0 & i\rho\beta^2\acute{\eta} & 0 & 0 & -1\\ 2i\rho\beta b\grave{\eta} & -i\rho\beta a & 0 & \beta p/r & -\beta\grave{\eta} & 0\\ 0 & 0 & i\rho\beta^2\grave{\eta} & 0 & 0 & 1\end{bmatrix}, \tag{36}$$

where $a=1-2\beta^2(p^2/r^2)$ and $b=\beta^2(p/r)$.

Following the formalism developed by Gilbert & Backus, the propagator **P** between radii r_1 and r_2 can be defined by

$$\mathbf{b}(r_2)=\mathbf{P}(r_2,r_1)\mathbf{b}(r_1)=\mathbf{D}(r_2)\mathbf{\Lambda}(r_2)\mathbf{\Lambda}^{-1}(r_1)\mathbf{D}^{-1}(r_1)\mathbf{b}(r_1). \tag{37}$$

In the same way and using eq. (29), we can define the propagator **S** to link the wave amplitudes between r_1 and r_2 by

$$\mathbf{a}(r_2)=\mathbf{S}(r_2,r_1)\mathbf{a}(r_1)=\mathbf{\Lambda}^{-1}(r_2)\mathbf{D}^{-1}(r_2)\mathbf{D}(r_1)\mathbf{\Lambda}(r_1)\mathbf{a}(r_1). \tag{38}$$

2.2.2 *The Green's function*

We are now going to use these propagators together with the boundary conditions and source terms to express the Green's function. Eq. (16) involves two Green's functions, one for the direct wave, and one for the scattered wave. The boundary conditions at the top of D″ are different for these two functions (see Fig. 3). On the other hand, they have the same lower boundary condition. Since the diffracted *S* waves are associated with the poles of the reflection coefficient at the CMB (Chapman & Phinney 1972; Cormier & Richards 1988), the lower boundary condition for both Green's functions reads

$$\begin{pmatrix}\grave{\mathbf{a}}_{\rm CMB}\\ \acute{\mathbf{a}}_{\rm CMB}\end{pmatrix}=\begin{pmatrix}\mathbf{I}_2\\ \mathbf{R}_{\rm CMB}\end{pmatrix}\grave{\mathbf{a}}_{\rm CMB}, \tag{39}$$

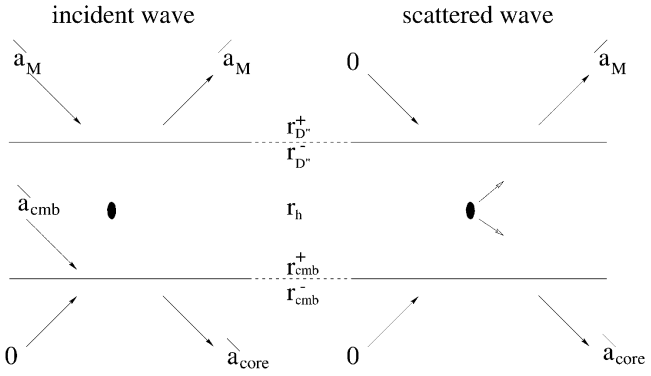

Figure 3. Detail of the boundary conditions used at the top of the D″ layer and in the core for the incident and scattered waves.

where $\mathbf{a}$ contains the amplitudes of the *SH* and *SV* waves propagating downwards and upwards in the bottom part of D″, $\mathbf{R}_{\mathrm{CMB}}$ is a diagonal matrix containing the reflection coefficients for the *SV* and *SH* waves at the CMB and $\mathbf{I}_2$ is the 2×2 identity matrix.

2.2.3 *Green's function for the incident wavefield*

For the direct wave, the source is located above D″, implying that there is both an incident wavefield on the top of D″ and a wavefield propagating upwards back into the lower mantle. The amplitudes $\mathbf{a}_{\mathrm{M}}$ above D″ are related to those $\mathbf{a}_{\mathrm{CMB}}$ in D″ by the propagator $\mathbf{S}$ (eq. 38):

$$\begin{pmatrix} \grave{\mathbf{a}}_{\mathrm{M}} \\ \acute{\mathbf{a}}_{\mathrm{M}} \end{pmatrix} = \mathbf{S}(r_{\mathrm{D}}^{+}, r_{\mathrm{D}}^{-}) \begin{pmatrix} \mathbf{I}_2 & \\ & \mathbf{R}_{\mathrm{CMB}} \end{pmatrix} \grave{\mathbf{a}}_{\mathrm{CMB}} . \tag{40}$$

Recall that, in the Langer approximation, the wave amplitudes are constant in each layer. r_{D} is the radius of the top of D″ and the $+/-$ signs indicate that the elements are evaluated right above or right below the top of D″. In the slowness range appropriate for this study, the elements evaluated at r_{D}^{-} can be calculated using the Langer approximation, and those evaluated at r_{D}^{+} can be calculated using the WKBJ approximation (Fig. 2). Decomposing the matrix $\mathbf{S}$ into four submatrices corresponding to the downgoing and upgoing directions of propagation,

$$\mathbf{S} = \begin{pmatrix} \mathbf{S}_{\mathrm{dd}} & \mathbf{S}_{\mathrm{du}} \\ \mathbf{S}_{\mathrm{ud}} & \mathbf{S}_{\mathrm{uu}} \end{pmatrix}, \tag{41}$$

eq. (40) can be used to express the total wavefield as a function of the incident waves only. We have

$$\grave{\mathbf{a}}_{\mathrm{CMB}} = (\mathbf{S}_{\mathrm{dd}} + \mathbf{S}_{\mathrm{du}}\mathbf{R}_{\mathrm{CMB}})^{-1} \grave{\mathbf{a}}_{\mathrm{M}} \tag{42}$$

and

$$\acute{\mathbf{a}}_{\mathrm{M}} = (\mathbf{S}_{\mathrm{ud}} + \mathbf{S}_{\mathrm{uu}}\mathbf{R}_{\mathrm{CMB}})\grave{\mathbf{a}}_{\mathrm{CMB}} , \tag{43}$$

and therefore

$$\acute{\mathbf{a}}_{\mathrm{M}} = \mathbf{R}_{\mathrm{D}''}\grave{\mathbf{a}}_{\mathrm{M}} , \tag{44}$$

with

$$\mathbf{R}_{\mathrm{D}''} = (\mathbf{S}_{\mathrm{ud}} + \mathbf{S}_{\mathrm{uu}}\mathbf{R}_{\mathrm{CMB}})(\mathbf{S}_{\mathrm{dd}} + \mathbf{S}_{\mathrm{du}}\mathbf{R}_{\mathrm{CMB}})^{-1} . \tag{45}$$

$\mathbf{R}_{\mathrm{D}''}$ is a diagonal matrix built up of the generalized reflection coefficients for *SV* and *SH* waves at the top of D″ in the laterally homogeneous model. It takes into account the reflection at the CMB as well as the whole propagation process within the D″ layer, including possible multiple reflections. The amplitudes of the waves above D″ can therefore be written as a function of the incident waves only:

$$\begin{pmatrix} \grave{\mathbf{a}}_{\mathrm{M}} \\ \acute{\mathbf{a}}_{\mathrm{M}} \end{pmatrix} = \begin{pmatrix} \mathbf{I}_2 \\ \mathbf{R}_{\mathrm{D}''} \end{pmatrix} \grave{\mathbf{a}}_{\mathrm{M}} . \tag{46}$$

These incident waves are generated by a source assumed to be located far above D″. This source is equivalent to a discontinuity in the displacement–stress vector $\Delta\mathbf{b}$ at a radius r_{s}. Up to a factor $\sqrt{(2l+1)/4\pi}\,(1/\omega r_{\mathrm{s}}^2)$ from eq. (24), we have

$$\Delta\mathbf{b} = \begin{bmatrix} 0 \\ -\mathbf{F} \end{bmatrix} . \tag{47}$$

This discontinuity corresponds to a discontinuity in the wave vector (Kennett 1983):

$$\Delta\mathbf{a} = \begin{bmatrix} -\grave{\mathbf{a}}_{\mathrm{s}} \\ \acute{\mathbf{a}}_{\mathrm{s}} \end{bmatrix} = \mathbf{\Lambda}^{-1}(r_{\mathrm{s}})\mathbf{D}^{-1}(r_{\mathrm{s}}) \begin{bmatrix} 0 \\ -\mathbf{F} \end{bmatrix} . \tag{48}$$

Assuming a simple downwards propagation, from the source level to the top of D″, we can then relate the amplitudes of the waves incident on D″ to the source terms:

$$\grave{\mathbf{a}}_{\mathrm{M}} = \grave{\mathbf{a}}_{\mathrm{s}} = \mathbf{T}_{\mathrm{d}}\mathbf{F} , \tag{49}$$

with

$$\mathbf{T}_{\mathrm{d}} = (\mathbf{I}_2 \quad 0)\mathbf{\Lambda}^{-1}(r_{\mathrm{s}})\mathbf{D}^{-1}(r_{\mathrm{s}}) \begin{pmatrix} 0 \\ \mathbf{I}_3 \end{pmatrix} , \tag{50}$$

where $\mathbf{I}_3$ is the 3×3 identity matrix. In this expression, $\mathbf{T}_{\mathrm{d}}$ is calculated using the WKBJ approximation. For clarity, we keep the vector $\mathbf{F}$ as the source term in this expression. In order to obtain the Green's functions, the vector $\mathbf{F}$ must ultimately be replaced by the 3×3 identity matrix.

Using eq. (46) and propagating the wavefield from the top of D″ to the depth r_{h} of the heterogeneity, we obtain the displacement associated with the wavefield incident on the heterogeneity,

$$\mathbf{u}(r_{\mathrm{h}}) = (\mathbf{I}_3 \quad 0)\mathbf{U}^{-1} \begin{pmatrix} \mathbf{I}_2 \\ \mathbf{R}_{\mathrm{D}''} \end{pmatrix} \mathbf{T}_{\mathrm{d}}\mathbf{F} , \tag{51}$$

with

$$\mathbf{U}^{-1} = \mathbf{D}(r_{\mathrm{h}})\mathbf{\Lambda}(r_{\mathrm{h}})\mathbf{S}^{-1}(r_{\mathrm{D}}^{+}, r_{\mathrm{D}}^{-}) . \tag{52}$$

Combining the spherical harmonics components, one obtains the Green's functions:

$$\mathbf{G}(r_{\mathrm{h}}, \theta) = \frac{1}{\omega r_{\mathrm{s}}^2} \sum_{l=0}^{\infty} \sqrt{\frac{2l+1}{4\pi}}\, \mathbf{u}(r_{\mathrm{h}})\, Y_l(\theta) . \tag{53}$$

Using $k = l + 1/2$ and eq. (19), this can be transformed into the wavenumber integration:

$$\mathbf{G}(r_{\mathrm{h}}, \Delta_{\mathrm{h-s}}) = \frac{1}{2\pi\omega r_{\mathrm{s}}^2} \int k\mathbf{u}(r_{\mathrm{h}}) Q^{(2)}(k\cos\Delta_{\mathrm{h-s}})\, dk , \tag{54}$$

where $\Delta_{\mathrm{h-s}}$ is the epicentral distance between the source and the heterogeneity (Fig. 2).

2.2.4 *Green's function for the scattered wavefield*

The scattered wavefield has its source at the location of the heterogeneity, in the D″ layer. Up to a factor $\sqrt{(2l+1)/4\pi}(1/\omega r_h^2)$, we have a discontinuity in the displacement–stress vector:

$$\Delta\mathbf{b} = \begin{bmatrix} 0 \\ -\mathbf{F} \end{bmatrix}, \tag{55}$$

where, as for the incident wavefield, we must ultimately replace $\mathbf{F}$ by the 3×3 identity matrix to obtain the Green's functions.

Using propagators to relate the boundary condition (39) at the CMB, the displacement–stress discontinuity at the source level, and the fact that there is no scattered wave propagating downwards above D″ (Fig. 3), we obtain the relation

$$\begin{pmatrix} 0 \\ \acute{\mathbf{a}}_M \end{pmatrix} = \mathbf{U}\begin{pmatrix} 0 \\ -\mathbf{F} \end{pmatrix} + \mathbf{S}\begin{pmatrix} \mathbf{I}_2 \\ \mathbf{R}_{CMB} \end{pmatrix}\grave{\mathbf{a}}_{CMB}, \tag{56}$$

where $\mathbf{U}$ is the inverse matrix defined in eq. (52). Decomposing $\mathbf{U}$ and $\mathbf{S}$ into submatrices, the system (56) can be decomposed into two subsystems:

$$0 = \mathbf{U}_{12}(-\mathbf{F}) + (\mathbf{S}_{dd} + \mathbf{S}_{du}\mathbf{R}_{CMB})\grave{\mathbf{a}}_{CMB}, \tag{57}$$

which gives the amplitudes at the CMB as a function of the source term,

$$\grave{\mathbf{a}}_{CMB} = (\mathbf{S}_{dd} + \mathbf{S}_{du}\mathbf{R}_{CMB})^{-1}\mathbf{U}_{12}\mathbf{F}, \tag{58}$$

which can be used in the second subsystem to obtain the amplitudes of the scattered waves at the top of D″ as a function of the source term only:

$$\acute{\mathbf{a}}_M = \mathbf{U}_{22}(-\mathbf{F}) + (\mathbf{S}_{ud} + \mathbf{S}_{uu}\mathbf{R}_{CMB})(\mathbf{S}_{dd} + \mathbf{S}_{du}\mathbf{R}_{CMB})^{-1}\mathbf{U}_{12}\mathbf{F}, \tag{59}$$

where we recognise the generalized reflection coefficient $\mathbf{R}_{D''}$ defined in eq. (45). The amplitude of the scattered wavefield above D″ therefore has the form

$$\acute{\mathbf{a}}_M = (\mathbf{R}_{D''} \quad -\mathbf{I}_2)\mathbf{U}\begin{pmatrix} 0 \\ \mathbf{F} \end{pmatrix}. \tag{60}$$

In the lower mantle, we can propagate this amplitude to any depth using a WKBJ propagator. The displacement at the receiver depth is equal to

$$\mathbf{u}(r_0) = \mathbf{T}_u\acute{\mathbf{a}}_M, \tag{61}$$

where

$$\mathbf{T}_u = (\mathbf{I}_3 \quad 0)\mathbf{D}(r_0)\mathbf{\Lambda}(r_0)\begin{pmatrix} 0 \\ \mathbf{I}_2 \end{pmatrix}. \tag{62}$$

The integration in wavenumber completes the calculation of the Green's function:

$$\mathbf{G}(r_0, \Delta_{r-h}) = \frac{1}{2\pi\omega r_h^2}\int k\mathbf{u}(r_0)Q^{(2)}(k\cos\Delta_{r-h})dk, \tag{63}$$

where Δ_{r-h} is the epicentral distance between the heterogeneity and the receiver.

2.3 Total scattered wavefield

Inserting the expressions for the Green's functions for the incident and scattered waves into eq. (16), we obtain the expression for the diffracted S wave scattered by a heterogeneity in D″:

$$\begin{aligned}\mathbf{u}^{scat} = \frac{1}{4\pi^2\omega^2 r_s^2 r_h^2}\int & k_{scat}\mathbf{T}_u(k_{scat})(\mathbf{R}_{D''}(k_{scat}) \quad -\mathbf{I}_2)\mathbf{U}(k_{scat}) \\ & \times \begin{pmatrix} 0 \\ \mathbf{I}_3 \end{pmatrix} Q^{(2)}(k_{scat}, \cos\Delta_{r-h})dk_{scat}\mathbf{\Delta M}\int k_{inc}(\mathbf{I}_3 \quad 0) \\ & \times \mathbf{U}^{-1}(k_{inc})\begin{pmatrix} \mathbf{I}_2 \\ \mathbf{R}_{D''}(k_{inc}) \end{pmatrix}\mathbf{T}_d(k_{inc})Q^{(2)}(k_{inc}, \cos\Delta_{h-s})dk_{inc},\end{aligned} \tag{64}$$

where we have made explicit the dependence on k of the different elements. k_{inc} is the wavenumber of the incident field and k_{scat} is the wavenumber of the scattered wavefield. An integral over ω is necessary to calculate the displacement in the time domain. The integrals over k_{inc}, k_{scat} and ω can be evaluated in any order. In practice, we have performed the integrals over ω last.

This expression is a combination of different elements with different functions. In order to emphasize these functions, we can reorganize eq. (64) in different ways. The propagator $\mathbf{U}$ can be separated into propagators

$$\mathbf{U} = \mathbf{S}\mathbf{W}_h, \quad \text{with} \quad \mathbf{W}_h = \mathbf{\Lambda}^{-1}(r_h)\mathbf{D}^{-1}(r_h). \tag{65}$$

Except for the factor $(1/\omega r_h^2)$, $\mathbf{W}_h$ contains all the elements that depend on the depth of the heterogeneity. $\mathbf{S}$ is the propagator used in eq. (45) to calculate the generalized reflection coefficients $\mathbf{R}_{D''}$. The scattered field can be rewritten as follows:

$$\begin{aligned}\mathbf{u}^{scat} = \frac{1}{4\pi^2\omega^2 r_s^2 r_h^2}\int\int & k_{scat}k_{inc}\mathbf{T}_u(k_{scat})(\mathbf{R}_{D''}(k_{scat}) \quad -\mathbf{I}_2)\mathbf{S}(k_{scat}) \\ & \times \mathbf{C}(k_{scat}, k_{inc})\mathbf{S}^{-1}(k_{inc})\begin{pmatrix} \mathbf{I}_2 \\ \mathbf{R}_{D''}(k_{inc}) \end{pmatrix}\mathbf{T}_d(k_{inc})dk_{scat}dk_{inc},\end{aligned} \tag{66}$$

where $\mathbf{C}$ is the coupling matrix at the level of the heterogeneity,

$$\begin{aligned}\mathbf{C}(k_{scat}, k_{inc}) = & Q^{(2)}(k_{scat}, \cos\Delta_{r-h})\mathbf{W}_h(k_{scat})\begin{pmatrix} 0 & 0 \\ \mathbf{\Delta M} & 0 \end{pmatrix} \\ & \times \mathbf{W}_h^{-1}(k_{inc})Q^{(2)}(k_{inc}, \cos\Delta_{h-s}).\end{aligned} \tag{67}$$

Recall that the differentiations in the coupling operator $\mathbf{\Delta M}$ are all with respect to the position of the heterogeneity. With this formulation, all the elements that depend on the location of the heterogeneity are grouped in the coupling matrix $\mathbf{C}$. This matrix expresses the coupling between different wave types and between different wavenumbers due to the presence of the inhomogeneity. It is built up of coupling coefficients between

different wave types:

$$\mathbf{C}(k_{\rm scat}, k_{\rm inc}) = Q^{(2)}(k_{\rm scat}, \cos\Delta_{\rm r-h}) \times \begin{pmatrix} SV^{\downarrow}_{\rm sc}SV^{\downarrow}_{\rm in} & SV^{\downarrow}_{\rm sc}SH^{\downarrow}_{\rm in} & SV^{\downarrow}_{\rm sc}SV^{\uparrow}_{\rm in} & SV^{\downarrow}_{\rm sc}SH^{\uparrow}_{\rm in} \\ SH^{\downarrow}_{\rm sc}SV^{\downarrow}_{\rm in} & SH^{\downarrow}_{\rm sc}SH^{\downarrow}_{\rm in} & SH^{\downarrow}_{\rm sc}SV^{\uparrow}_{\rm in} & SH^{\downarrow}_{\rm sc}SH^{\uparrow}_{\rm in} \\ SV^{\uparrow}_{\rm sc}SV^{\downarrow}_{\rm in} & SV^{\uparrow}_{\rm sc}SH^{\downarrow}_{\rm in} & SV^{\uparrow}_{\rm sc}SV^{\uparrow}_{\rm in} & SV^{\uparrow}_{\rm sc}SH^{\uparrow}_{\rm in} \\ SH^{\uparrow}_{\rm sc}SV^{\downarrow}_{\rm in} & SH^{\uparrow}_{\rm sc}SH^{\downarrow}_{\rm in} & SH^{\uparrow}_{\rm sc}SV^{\uparrow}_{\rm in} & SH^{\uparrow}_{\rm sc}SH^{\uparrow}_{\rm in} \end{pmatrix} \times Q^{(2)}(k_{\rm inc}, \cos\Delta_{\rm h-s}), \quad (68)$$

where the element $SV^{\uparrow}_{\rm sc}SV^{\downarrow}_{\rm in}$, for example, corresponds to the coupling between a downgoing incident field polarized in SV, denoted $SV^{\downarrow}_{\rm in}$, and an upgoing scattered field with the same polarization, denoted $SV^{\uparrow}_{\rm sc}$. We will analyse this matrix in detail in the next section. We here note that the matrix contains elements for both downgoing and upgoing incident fields, as well as downgoing and upgoing scattered fields. This expresses, for example, the fact that the incident wavefield may reach the heterogenity from above, or from below after reflection on the CMB.

The terms $\mathbf{T}_{\rm d}$ and $\mathbf{T}_{\rm u}$ express the propagation in the lower mantle from the source to the top of D″, and from the top of D″ to the receiver. They are simple terms that are not of special interest in our problem. We can isolate them from the elements that relate to the propagation and scattering within D″ and rewrite eq. (64) as

$$\mathbf{u}^{\rm scat} = \frac{1}{4\pi^2\omega^2 r_{\rm s}^2 r_{\rm h}^2}\int\int k_{\rm scat}k_{\rm inc}\mathbf{T}_{\rm u}(k_{\rm scat})\mathbf{\Omega}_{\rm D''}\mathbf{T}_{\rm d}(k_{\rm inc})dk_{\rm scat}dk_{\rm inc}\,, \quad (69)$$

where

$$\mathbf{\Omega}_{\rm D''} = (\mathbf{R}_{\rm D''}(k_{\rm scat}) \quad -\mathbf{I}_2)\mathbf{S}(k_{\rm scat}) \times \mathbf{C}(k_{\rm scat}, k_{\rm inc})\mathbf{S}^{-1}(k_{\rm inc})\begin{pmatrix}\mathbf{I}_2\\ \mathbf{R}_{\rm D''}(k_{\rm inc})\end{pmatrix}. \quad (70)$$

Using eqs (49) and (61), one can see that $\mathbf{\Omega}_{\rm D''}$ expresses the relation between the wavefield entering D″ from the lower mantle and the wavefield leaving D″, scattered by the heterogeneity:

$$\mathbf{\acute{a}}_{\rm M}(k_{\rm scat}) = \mathbf{\Omega}_{\rm D''}(k_{\rm scat}, k_{\rm inc})\mathbf{\grave{a}}_{\rm M}(k_{\rm inc}), \quad (71)$$

with

$$\mathbf{\Omega}_{\rm D''}(k_{\rm scat}, k_{\rm inc}) = \begin{pmatrix} \Omega_{SV^{\uparrow}_{\rm sc}SV^{\downarrow}_{\rm in}} & \Omega_{SV^{\uparrow}_{\rm sc}SH^{\downarrow}_{\rm in}} \\ \Omega_{SH^{\uparrow}_{\rm sc}SV^{\downarrow}_{\rm in}} & \Omega_{SH^{\uparrow}_{\rm sc}SH^{\downarrow}_{\rm in}} \end{pmatrix}. \quad (72)$$

$\mathbf{\Omega}_{\rm D''}$ is a matrix of generalized reflection coefficients at the top of the D″ layer. It models the whole process that occurs below the top of D″; that is, coupling due to the inhomogeneity, reflection at the CMB, propagation and possible tunnelling in D″. We note that this reflection coefficient matrix is not diagonal. Like the coupling matrix $\mathbf{C}$, it expresses the fact that the heterogeneity produces coupling between different wavenumbers and between SH and SV waves. However, in contrast to the coupling matrix $\mathbf{C}$, the reflection coefficients are calculated only for downgoing incident wavefields and upgoing scattered wavefields.

2.4 Analysis of the coupling matrix C

In the following, we detail the calculation of an element of $\mathbf{C}$ defined by eq. (67). We then specify the general form of the other terms, which are given in Appendix A, and analyse the properties of the coupling matrix. Let us consider the element $SV^{\uparrow}_{\rm sc}SV^{\downarrow}_{\rm in}$. Using eqs (30), (35) and (36) for $\mathbf{\Lambda}$, $\mathbf{\Lambda}^{-1}$, $\mathbf{D}$ and $\mathbf{D}^{-1}$, we obtain

$$C_{SV^{\uparrow}_{\rm sc}SV^{\downarrow}_{\rm in}} = \frac{-i\omega^2 r_{\rm h}^2}{2\rho_{\rm h}\beta_{\rm h}^3}Q^{(2)}[k_{\rm sc}, \cos(\theta_r-\theta_{\rm h})]\grave{\sigma}_{\rm sc}(\beta p_{\rm sc}/r_{\rm h} \quad -\beta\grave{\eta}_{\rm sc} \quad 0) \times \mathbf{\Delta M}\begin{pmatrix}\beta p_{\rm in}/r_{\rm h}\\ \beta\grave{\eta}_{\rm in}\\ 0\end{pmatrix}\grave{\sigma}_{\rm in}Q^{(2)}[k_{\rm in}, \cos(\theta_{\rm h}-\theta_{\rm s})]. \quad (73)$$

Recall that, in the matrix $\mathbf{\Lambda}$, $\grave{\boldsymbol{\sigma}}$ and $\acute{\boldsymbol{\sigma}}$ correspond respectively to the down- and upgoing radial wave functions. On the other hand, in the matrix $\mathbf{\Lambda}^{-1}$ the correspondence is inverted (see eq. 30): that is why $\grave{\sigma}_{\rm sc}$ appears in eq. (73) for the upgoing scattered wave. We have chosen to work in a frame of reference independent of the great-circle paths between source–heterogeneity and heterogeneity–receiver in order to check that only the angle $\Psi = \phi_2 - \phi_1$ (see Fig. 1) appears in the coupling matrix (Snieder 1986a). This frame of reference is denoted ($\hat{\boldsymbol{r}}$, $\hat{\boldsymbol{x}}$, $\hat{\boldsymbol{y}}$), where the direction x corresponds to north, the direction y to east and the angles ϕ_1 and ϕ_2 to the azimuthal angles. In this new frame of reference, eq. (73) becomes

$$C_{SV^{\uparrow}_{\rm sc}SV^{\downarrow}_{\rm in}} = \frac{-i\omega^2 r_{\rm h}^2}{2\rho_{\rm h}\beta_{\rm h}^3}Q^{(2)}[k_{\rm sc}, \cos(\theta_r-\theta_{\rm h})]\grave{\sigma}_{\rm sc} \times (\beta p_{\rm sc}/r_{\rm h} \quad -\beta\grave{\eta}_{\rm sc}\cos\phi_2 \quad -\beta\grave{\eta}_{\rm sc}\sin\phi_2) \times \mathbf{\Delta M}\begin{pmatrix}\beta p_{\rm in}/r_{\rm h}\\ \beta\grave{\eta}_{\rm in}\cos\phi_1\\ \beta\grave{\eta}_{\rm in}\sin\phi_1\end{pmatrix}\grave{\sigma}_{\rm in}Q^{(2)}[k_{\rm in}, \cos(\theta_{\rm h}-\theta_{\rm s})]. \quad (74)$$

This expression involves the derivatives of the Green's function with respect to $r_{\rm h}$, $\theta_{\rm h}$ and $\phi_{1,2}$. Since the Langer approximation is a high-frequency approximation, we only need to keep the higher terms in ω. We can thus neglect, in the derivatives with respect to $r_{\rm h}$, the terms other than those in $d\acute{\boldsymbol{\sigma}}/dr_{\rm h}$ and $d\grave{\boldsymbol{\sigma}}/dr_{\rm h}$. Those can be calculated with the help of the radial slownesses $\acute{\eta}$ and $\grave{\eta}$ (eq. 33):

$$\frac{d\acute{\boldsymbol{\sigma}}(r_{\rm h})}{dr_{\rm h}} = i\omega\acute{\eta}\acute{\boldsymbol{\sigma}}(r_{\rm h}), \quad \frac{d\grave{\boldsymbol{\sigma}}(r_{\rm h})}{dr_{\rm h}} = -i\omega\grave{\eta}\grave{\boldsymbol{\sigma}}(r_{\rm h}). \quad (75)$$

The derivatives with respect to $\theta_{\rm h}$ at highest order in ω are

$$\frac{d}{d\theta_{\rm h}}Q^{(2)}[k_{\rm in}, \cos(\theta_{\rm h}-\theta_{\rm s})] = i\omega p_{\rm in}Q^{(2)}[k_{\rm in}, \cos(\theta_{\rm h}-\theta_{\rm s})],$$

$$\frac{d}{d\theta_{\rm h}}Q^{(2)}[k_{\rm sc}, \cos(\theta_r-\theta_{\rm h})] = -i\omega p_{\rm sc}Q^{(2)}[k_{\rm sc}, \cos(\theta_r-\theta_{\rm h})]. \quad (76)$$

The derivatives with respect to ϕ_1 or ϕ_2 have no ω factor and can thus be neglected, as in the case of the coupling of surface waves by an inhomogeneity (Snieder 1986a; Snieder & Nolet 1987).

In the frame of reference ($\hat{\boldsymbol{r}}$, $\hat{\boldsymbol{x}}$, $\hat{\boldsymbol{y}}$) (Fig. 1) we need the derivatives with respect to x and y:

$$\frac{df}{dx} = \frac{1}{r_h}\cos\phi\,\frac{df}{d\theta}\,, \quad \frac{df}{dy} = \frac{1}{r_h}\sin\phi\,\frac{df}{d\theta}\,. \tag{77}$$

To be concise, we use the following notations: $R_1 = SV_{in}^{\downarrow}$ and $R_2 = SV_{sc}^{\uparrow}$. We factorize out of the expression of the coupling coefficient (eq. 73) the terms $(-i\omega^2 r_h^2/2\rho_h\beta_h^3)Q_l^{(2)}\times[k_{sc}, \cos(\theta_r-\theta_h)]\dot{\sigma}_{sc}$ and $\dot{\sigma}_{in}Q_l^{(2)}[k_{in}, \cos(\theta_h-\theta_s)]$. As can be seen in eqs (67) and (73), only part of the matrices $\mathbf{D}$ and $\mathbf{D}^{-1}$ intervenes in the calculation of coupling elements. However, for the sake of clarity, we will use $\mathbf{D}$ and $\mathbf{D}^{-1}$ in the following. The coupling by itself can be written as a sum of four terms.

(1) *Term in* $\Delta\rho$*:*

$$\begin{aligned}
&\Delta\rho\omega^2 D_{R_2k}^{-1} D_{kR_1}\\
&\quad = \Delta\rho\omega^2 V_h[D_{R_2r}^{-1}D_{rR_1} + D_{R_2x}^{-1}D_{xR_1} + D_{R_2y}^{-1}D_{yR_1}]\\
&\quad = \Delta\rho\omega^2 V_h[(\beta p_{sc}/r_h)(\beta p_{in}/r_h) + (-\beta\dot{\eta}_{sc})(\beta\dot{\eta}_{in})\cos(\phi_2-\phi_1)]\,.
\end{aligned} \tag{78}$$

(2) *Term in* $-\Delta\lambda$*:*

$$\begin{aligned}
&(-\Delta\lambda)V_h[\partial_j^h D_{R_2j}^{-1}][\partial_k^h D_{kR_1}]\\
&\quad = (-\Delta\lambda)V_h[\partial_r^h D_{R_2r}^{-1} + \partial_x^h D_{R_2x}^{-1} + \partial_y^h D_{R_2y}^{-1}]\\
&\qquad \times[\partial_r^h D_{rR_1} + \partial_x^h D_{xR_1} + \partial_y^h D_{yR_1}]\\
&\quad = (-\Delta\lambda)V_h[(\beta p_{sc}/r_h)(-i\omega\dot{\eta}_{sc})\\
&\qquad + (-\beta\dot{\eta}_{sc})(-i\omega p_{sc}/r_h)(\cos^2\phi_2 + \sin^2\phi_2)]\\
&\qquad \times[(\beta p_{in}/r_h)(-i\omega\dot{\eta}_{in}) + (\beta\dot{\eta}_{in})(i\omega p_{in}/r_h)(\cos^2\phi_1 + \sin^2\phi_1)]\\
&\quad = 0\,.
\end{aligned} \tag{79}$$

This result is in agreement with the fact that a perturbation in $\Delta\lambda$ does not couple the S polarizations (Wu & Aki 1985).

(3) *First term in* $-\Delta\mu$*:*

$$\begin{aligned}
&(-\Delta\mu)V_h[\partial_k^h D_{R_2j}^{-1}][\partial_j^h D_{kR_1}]\\
&\quad = (-\Delta\mu)V_h[\partial_r^h D_{R_2r}^{-1}\partial_r^h D_{rR_1} + \partial_r^h D_{R_2x}^{-1}\partial_x^h D_{rR_1} + \partial_r^h D_{R_2y}^{-1}\partial_y^h D_{rR_1}\\
&\qquad \times\partial_x^h D_{R_2r}^{-1}\partial_r^h D_{xR_1} + \partial_x^h D_{R_2x}^{-1}\partial_x^h D_{xR_1} + \partial_x^h D_{R_2y}^{-1}\partial_y^h D_{xR_1}\\
&\qquad \times\partial_y^h D_{R_2r}^{-1}\partial_r^h D_{yR_1} + \partial_y^h D_{R_2x}^{-1}\partial_x^h D_{yR_1} + \partial_y^h D_{R_2y}^{-1}\partial_y^h D_{yR_1}]\\
&\quad = (-\Delta\mu)V_h[(\beta p_{sc}/r_h)(-i\omega\dot{\eta}_{sc})(\beta p_{in}/r_h)(-i\omega\dot{\eta}_{in})\\
&\qquad + [(-\beta\dot{\eta}_{sc})(-i\omega\dot{\eta}_{sc})(\beta\dot{\eta}_{in})(-i\omega\dot{\eta}_{in})\\
&\qquad + (\beta p_{sc}/r_h)(-i\omega p_{sc}/r_h)(\beta p_{in}/r_h)(i\omega p_{in}/r_h)]\cos(\phi_2-\phi_1)\\
&\qquad + (-i\omega p_{sc}/r_h)(i\omega p_{in}/r_h)(-\beta\dot{\eta}_{sc})(\beta\dot{\eta}_{in})\cos^2(\phi_2-\phi_1)]\,.
\end{aligned} \tag{80}$$

(4) *Second term in* $-\Delta\mu$*:*

$$\begin{aligned}
&(-\Delta\mu)V_h[\partial_k^h D_{R_2j}^{-1}][\partial_k^h D_{jR_1}]\\
&\quad = (-\Delta\mu)V_h[\partial_r^h D_{R_2r}^{-1}\partial_r^h D_{rR_1} + \partial_r^h D_{R_2x}^{-1}\partial_r^h D_{xR_1} + \partial_r^h D_{R_2y}^{-1}\partial_r^h D_{yR_1}\\
&\qquad \times\partial_x^h D_{R_2r}^{-1}\partial_x^h D_{rR_1} + \partial_x^h D_{R_2x}^{-1}\partial_x^h D_{xR_1} + \partial_x^h D_{R_2y}^{-1}\partial_x^h D_{yR_1}\\
&\qquad \times\partial_y^h D_{R_2r}^{-1}\partial_y^h D_{rR_1} + \partial_y^h D_{R_2x}^{-1}\partial_y^h D_{xR_1} + \partial_y^h D_{R_2y}^{-1}\partial_y^h D_{yR_1}]\\
&\quad = (-\Delta\mu)V_h[(\beta p_{sc}/r_h)(-i\omega\dot{\eta}_{sc})(\beta p_{in}/r_h)(-i\omega\dot{\eta}_{in})\\
&\qquad + [(-\beta\dot{\eta}_{sc})(-i\omega\dot{\eta}_{sc})(\beta\dot{\eta}_{in})(-i\omega\dot{\eta}_{in})\\
&\qquad + (\beta p_{sc}/r_h)(-i\omega p_{sc}/r_h)(\beta p_{in}/r_h)(i\omega p_{in}/r_h)]\cos(\phi_2-\phi_1)\\
&\qquad + (-i\omega p_{sc}/r_h)(i\omega p_{in}/r_h)(-\beta\dot{\eta}_{sc})(\beta\dot{\eta}_{in})\cos^2(\phi_2-\phi_1)]\,.
\end{aligned} \tag{81}$$

(5) *Summary (we set* $\Psi = \phi_2 - \phi_1$*):*

$$\begin{aligned}
C_{SV_{sc}^{\uparrow}SV_{in}^{\downarrow}} = {}& \frac{-i\omega^2 r_h^2}{2\rho_h\beta_h^3}\,Q^{(2)}[k_{sc}, \cos(\theta_r-\theta_h)]\dot{\sigma}_{sc}V_h\\
&\times[\Delta\rho\omega^2(\beta p_{sc}/r_h)(\beta p_{in}/r_h)\\
&-3\Delta\mu(\beta p_{sc}/r_h)(-i\omega\dot{\eta}_{sc})(\beta p_{in}/r_h)(-i\omega\dot{\eta}_{in})\\
&+\cos\Psi[\Delta\rho\omega^2(-\beta\dot{\eta}_{sc})(\beta\dot{\eta}_{in})\\
&-\Delta\mu[(-\beta\dot{\eta}_{sc})(-i\omega\dot{\eta}_{sc}) + (\beta p_{sc}/r_h)(-i\omega p_{sc}/r_h)]\\
&\times[(\beta\dot{\eta}_{in})(-i\omega\dot{\eta}_{in}) + (\beta p_{in}/r_h)(i\omega p_{in}/r_h)]]\\
&-\cos 2\Psi\Delta\mu(-i\omega p_{sc}/r_h)(i\omega p_{in}/r_h)(-\beta\dot{\eta}_{sc})(\beta\dot{\eta}_{in})]\\
&\times\dot{\sigma}_{in}Q^{(2)}[k_{in}, \cos(\theta_h-\theta_s)]\,.
\end{aligned} \tag{82}$$

This expression is very similar to that obtained by Snieder (1986a) for surface waves.

2.4.1 *General form of the coefficients of the coupling matrix*

Completing this with the other elements of the coupling matrix presented in Appendix A, we can write the coupling coefficients between the different wave types in a general and compact form by not specifying the directions of wave propagation. For example, η_{sc} may correspond to either $\dot{\eta}_{sc}$, or $\acute{\eta}_{sc}$, and similarly for η_{in}, σ_{sc} and σ_{in}.

(1) *Case* $SV_{sc}SV_{in}$*:*

$$\begin{aligned}
C_{SV_{sc}SV_{in}} = {}& \frac{-i\omega^2 r_h^2}{2\rho_h\beta_h^3}\,Q^{(2)}[k_{sc}, \cos(\theta_r-\theta_h)]\sigma_{sc}V_h\\
&\times[\Delta\rho n_1(k_{sc}, k_{in}) - 3\Delta\mu n_2(k_{sc}, \eta_{sc}, k_{in}, \eta_{in})\\
&+\cos\Psi(\Delta\rho n_3(\eta_{sc}, \eta_{in}) - \Delta\mu n_4(k_{sc}, \eta_{sc}, k_{in}, \eta_{in}))\\
&-\cos 2\Psi\Delta\mu n_5(k_{sc}, \eta_{sc}, k_{in}, \eta_{in})]\sigma_{in}Q^{(2)}\\
&\times[k_{in}, \cos(\theta_h-\theta_s)]\,.
\end{aligned} \tag{83}$$

(2) *Case* $SV_{sc}SH_{in}$:

$$C_{SV_{sc}SH_{in}} = \frac{-i\omega^2 r_h^2}{2\rho_h \beta_h^3} Q^{(2)}[k_{sc}, \cos(\theta_r - \theta_h)]\sigma_{sc} V_h \times [\sin\Psi(\Delta\rho n_6(\eta_{sc}) - \Delta\mu n_7(k_{sc}, \eta_{sc}, \eta_{in})) - \sin 2\Psi \Delta\mu n_8(k_{sc}, \eta_{sc}, k_{in})]\sigma_{in} Q^{(2)}[k_{in}, \cos(\theta_h - \theta_s)]. \quad (84)$$

(3) *Case* $SH_{sc}SV_{in}$:

$$C_{SH_{sc}SV_{in}} = \frac{-i\omega^2 r_h^2}{2\rho_h \beta_h^3} Q^{(2)}[k_{sc}, \cos(\theta_r - \theta_h)]\sigma_{sc} V_h \times [(-\sin\Psi)(\Delta\rho n_9(\eta_{in}) - \Delta\mu n_{10}(\eta_{sc}, k_{in}, \eta_{in})) - (-\sin 2\Psi)\Delta\mu n_{11}(k_{sc}, k_{in}, \eta_{in})]\sigma_{in} Q^{(2)} \times [k_{in}, \cos(\theta_h - \theta_s)]. \quad (85)$$

(4) *Case* $SH_{sc}SH_{in}$:

$$C_{SH_{sc}SH_{in}} = \frac{-i\omega^2 r_h^2}{2\rho_h \beta_h^3} Q^{(2)}[k_{sc}, \cos(\theta_r - \theta_h)]\sigma_{sc} V_h \times [\cos\Psi(\Delta\rho n_{12} - \Delta\mu n_{13}(\eta_{sc}, \eta_{in})) - \cos 2\Psi \Delta\mu n_{14}(k_{sc}, k_{in})]\sigma_{in} Q^{(2)}[k_{in}, \cos(\theta_h - \theta_s)]. \quad (86)$$

n_1 to n_{14} are defined in Appendix A.

2.4.2 *Analysis of the coupling matrix*

(1) As for plane waves, the interaction of the wavefield with an inhomogeneity, characterized by a perturbation in $\Delta\rho$ or $\Delta\mu$, introduces a coupling between wavenumbers and wave types (*SV* and *SH*). A factor ω^2 is present in all terms, implying that the scattered wave spectrum equals the incident wave spectrum multiplied by ω^2 in the case of Rayleigh diffusion (Aki & Richards 1980b).

(2) A heterogeneity in $\Delta\lambda$ has no influence on *S* waves. This result is well known since the secondary force which corresponds to this type of perturbation is an explosion (Wu & Aki 1985).

(3) The polarization vectors for *SV* and *SH* depend on the azimuthal angles ϕ_1 and ϕ_2 separately, while the coupling matrix depends only on the scattering angle $\Psi = \phi_2 - \phi_1$ (Snieder 1986a). In ray theory, it is usual to define the scattering angle as the angle between the incident and scattered rays. In the Langer approximation, the incidence angle *i* with respect to the vertical is taken into account in the horizontal ray parameter *p* and in the radial slownesses η. Consequently, the angle Ψ characterizes the angular difference between the vertical plane containing the incident ray and the vertical plane containing the scattered ray (Fig. 1).

(4) There is no conversion between *SV* and *SH* waves in the forward ($\Psi = 0$) and backward ($\Psi = \pi$) directions. More generally, the coupling between wavetypes varies in $\sin\Psi$ and $\sin 2\Psi$, whereas coupling between waves of the same type varies in $\cos\Psi$ and $\cos 2\Psi$. This is a well-known property of *S* waves (Wu & Aki 1985) and surface waves (Snieder 1986a).

3 RESULTS

In this section, we analyse the characteristics of scattered S_{diff} waves for some simple models such as a vertical plume, a localized low-velocity zone and small inhomogeneities distributed in a random way in the D″ layer.

3.1 Computational aspects

When developing the software for the synthesis of the waveforms presented in the next sections, we have greatly benefited from the program package of Cormier & Richards (1988) for the spectral synthesis of body waves in a radially symmetric medium. To include the scattering effects, we have effectively programmed the matrix $\mathbf{\Omega}_{D''}(k_{scat}, k_{inc})$ defined by eq. (70). Depending on the values of k_{scat} and k_{inc}, $\mathbf{\Omega}_{D''}(k_{scat}, k_{inc})$ is calculated with two different bases of vertical wave functions. Following Kennett & Illingworth, we choose the basis with the stationary wave ($\check{\boldsymbol{\sigma}}$, $\check{\sigma}$) if the ray turns above the heterogeneity, otherwise we choose the basis with the propagating waves ($\check{\boldsymbol{\sigma}}$, $\acute{\boldsymbol{\sigma}}$) (see Section 2.2). This choice is very important to stabilize the numerical results. Eq. (69) for the scattered wavefield involves a double integration over wavenumbers k_{inc} and k_{scat}. We use the same domains for k_{inc} and k_{scat}. The integration domains are deformed in the complex plane around the poles of the diffracted waves. Along the real axis, the slowness runs from 458.4 s rad^{-1} to 509.9 s rad^{-1} in most cases, and to 521.4 s rad^{-1} for model 1 (see below) and heterogeneities located at a radius of larger than 3535 km. Integration domains away from the real axis depend on the model, the heterogeneity depth and the frequency. See to Emery (1997) for further details. Numerical problems related to growing exponentials and large arguments $\omega\tau$ of the Airy functions (eqs 31 and 32) increase with frequency. We must therefore limit the calculation of the scattered wavefield to periods greater than 4 s. Characteristic periods of diffracted *S* waves, between 8 and 20 s, are well within our frequency domain.

Calculations are performed in purely elastic models. The effect of causal attenuation is added to the waveforms using the integral along their ray path of a frequency-independent quality factor. They are convolved with the response of an IRIS broad-band instrument (station HRV). Source depth is 540 km and various source types will be used in the following (see Table 1). We use two different background velocity models. The first (model 1, see Fig. 4) is a modification of PREM (Dziewonski & Anderson 1981), with a 300 km thick D″ layer (instead of 150 km in PREM). Model 2 is characterized by a negative gradient (-0.00088 s^{-1}), which is a realistic model for a path that samples D″ under the Pacific (Garnero *et al.* 1988; Ritsema *et al.* 1997).

Heterogeneities have been parametrized by percentages of relative velocity and density perturbations. We have considered velocity perturbation rather than shear modulus perturbations in order to facilitate comparisons with tomographic models. A systematic study for various scatterer positions and both background velocity models has shown that scattered wave amplitudes for a unit velocity perturbation are larger by at least a factor of 10 than scattered wave amplitudes for a unit density perturbation (Emery 1997). Consequently, in the following we will only take into account velocity perturbations (and $\Delta\rho/\rho = 0$ per cent).

Table 1. Various sources used in our calculation to obtain different SV and SH amplitudes on the great-circle path between source and receiver.

Amplitudes on great-circle path	Source						
	date	az	baz				
$SV \simeq SH$	860526	52°	267,7°				
	Moment tensor	MRR	MTT	MFF	MRT	MRF	MTF
		−0,10	1,36	−1,26	−5,08	0,99	1,60
zero SV	strike	dip	rake	az			
maximum SH	0°	90°	0°	90°			
maximum SV	strike	dip	rake	az			
zero SH	0°	90°	90°	90°			

The theory developed in the previous sections is based on point heterogeneities. In practice, we found by analysing how the phase of the scattered wavefield varies with the position of the heterogeneity that elementary bricks that have a 2° horizontal dimension (that is, about 120 km at the CMB level) and 10 km thickness can be considered as point heterogeneities for diffracted S waves. For larger heterogeneities we divided the volume into elementary bricks, calculated the scattered fields for the different bricks, and added them together.

In the following, we conduct a study of the evolution of the amplitude ratio between the scattered wave and the direct wave with epicentral distance. The background velocity model is model 1. For each epicentral distance, the inhomogeneity is located at the centre of the great-circle path between the source and the receiver, just above the CMB for distances larger than 100°, and at the depth corresponding to the turning point for other distances. The wave amplitudes are measured on seismograms convolved with a broad-band instrument response and low-pass filtered. In the Born approximation, the amplitude of the scattered field for a single heterogeneity is a linear combination of its volume and its strength. For Fig. 5, we choose elementary brick heterogeneities ($V_h = 120 \times 120 \times 10$ km^3) and $\Delta\beta/\beta = -10$ per cent. We observe that the amplitude of the scattered wave is very weak, less than 1 per cent of the amplitude of the direct wave. Amplitudes of the same order of magnitude have been found by Ji & Nataf (1998a) for P waves. The two polarizations appear to behave differently: SH_{scat}/SH_{direct} is greater than SV_{scat}/SV_{direct} when the waves are diffracted ($\Delta \geq 100°$).

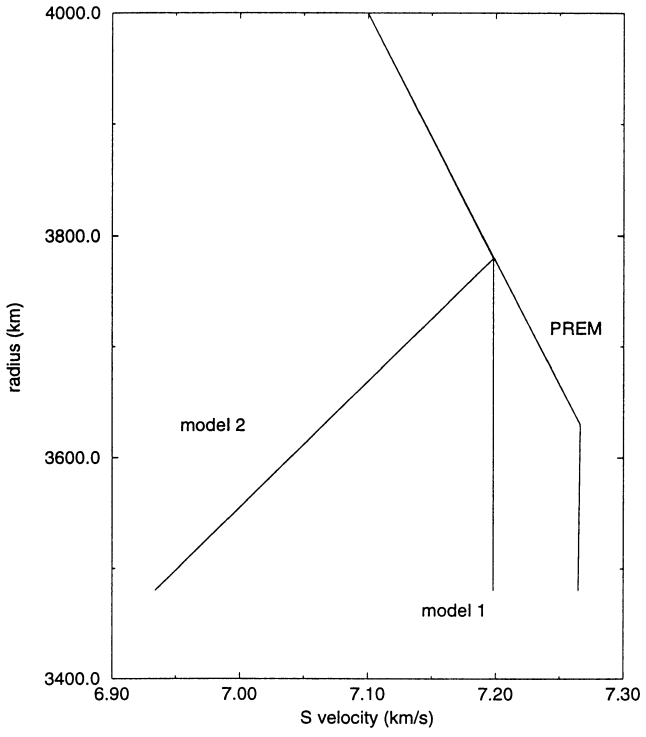

Figure 4. Velocity models used in the calculations. The thickness of D″ is 300 km; lower mantle velocities are unchanged from PREM. Model 1 has no velocity gradient, model 2 a negative velocity gradient of -0.00088 s^{-1}.

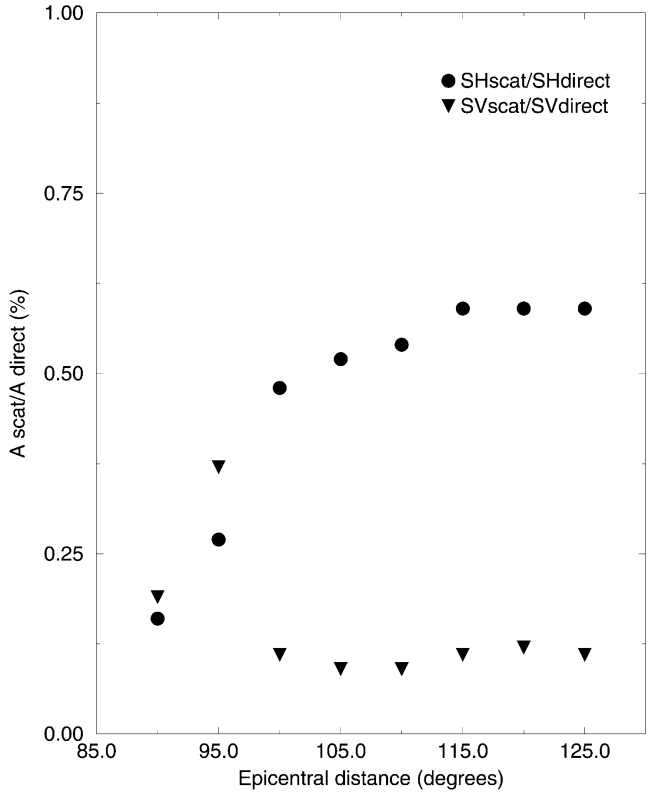

Figure 5. Amplitude ratio between the scattered wave and the direct wave for different epicentral distances. The volume of the heterogeneity is $V_h = 120 \times 120 \times 10$ km^3 and its strength $\Delta\beta/\beta = -10$ per cent. The source is 860526 (Table 1). We note a greater ratio for SH_{scat}/SH_{direct} than for SV_{scat}/SV_{direct}.

We note that the *SV* and *SH* wavefields show somewhat different sensitivities to the depth of the heterogeneity. We find that the *SH* wavefields are more sensitive to heterogeneities closer to the CMB, in accordance with the results of Doornbos & Mondt (1979a). In the model with a gradient, the scattered *SH* waves have their largest amplitudes when the heterogeneities are situated in a 100 km thick zone above the CMB, whereas the *SV* scattered waves reach maximum amplitudes for heterogeneities situated at the top of that zone. In the model without a gradient, the situation is similar but with a 200 km thick zone. By putting the heterogeneity somewhat further away from the CMB, we would have obtained amplitudes ratios 10 times larger for the *SV* components at 110° of epicentral distance and 15 times larger at 120° in Fig. 5.

3.2 Heterogeneity along the great-circle path

We first concentrate our attention on heterogeneous areas situated along the great-circle path between the source and the receiver. We consider two different heterogeneous models: an inhomogeneous area that is 2° wide and extends 10° along the great-circle path with $\Delta\beta/\beta = -10$ per cent; in the second model, the inhomogeneous area extends over 20° and $\Delta\beta/\beta = -5$ per cent. In both cases, the heterogeneous area is 30 km thick (Fig. 6). We note that the two models have the same volume times strength of heterogeneity. By comparing the scattering produced in the two models, we want to check whether or not the diffracted waves can resolve the difference between the two models.

The results are presented in Fig. 7 for background model 1 and Fig. 8 for background model 2. Although the source is chosen such that the amplitudes of *SH* and *SV* waves at the source level are nearly equal, we note in Fig. 7 the strong attenuation of the scattered SV_{diff} compared to the scattered SH_{diff} at both epicentral distances (110° and 120°). When a low-velocity zone is added at the base of the mantle, the diffraction phenomena is strengthened (in Fig. 8 we note stronger amplitudes and late arrival times for scattered waves) compared to the case with no negative velocity gradient (Fig. 7). With a positive velocity gradient in the D″ region, the SV_{diff} wave would have disappeared at these epicentral distances.

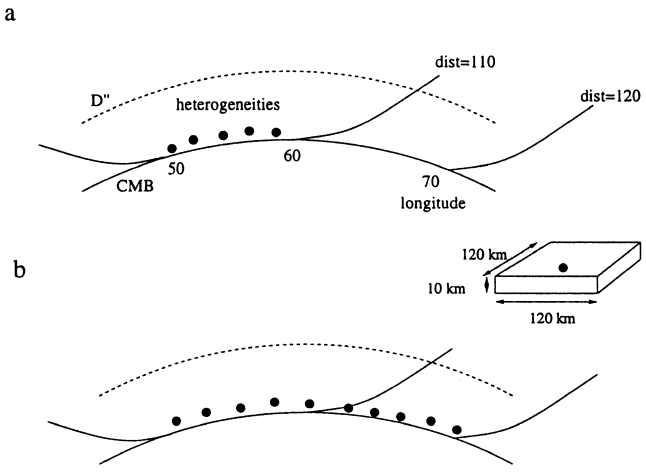

Figure 6. Two cases considered: (a) −10 per cent velocity perturbation along 10°; (b) −5 per cent velocity perturbation along 20°.

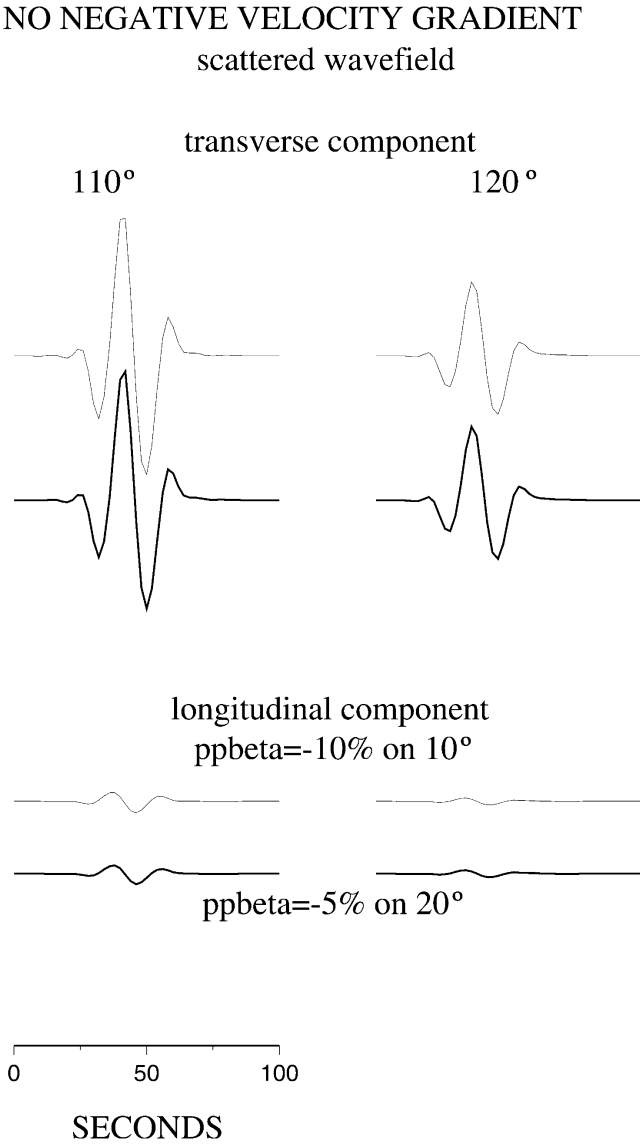

Figure 7. Scattered waves for the models depicted in Fig. 6 (case a shown as thin lines and b as thick lines). The background velocity model has no gradient in the D″ layer (model 1). The source is event 860526 (Table 1); origin time $t_0 = 1470$ s for $\Delta = 110°$ and $t_0 = 1560$ s for $\Delta = 120°$. The two models produce very similar scattered waves at both epicentral distances (difference in amplitude at most 10 per cent).

The two models presented in Fig. 6 produce nearly the same scattered wavefield. For both distances, we can see a maximum amplitude difference of 5 per cent for SH_{diff} and 10 per cent for SV_{diff} between the two cases. For $\Delta = 120°$, the geometrical diffracted line along the CMB is at distances from the source of between 50° and 70° (see Fig. 6), that is, in the region where the heterogeneity is located. As the phase variation of the scattered field is small in the volume of the heterogeneity, the amplitude of the scattered wavefield is a rather linear combination of the volume and strength of the heterogeneity. It is therefore not surprising that both models result in similar scattered wavefields at $\Delta = 120°$. It is more surprising for $\Delta = 110°$, because the geometrical diffracted zone spreads only over 10° (Fig. 6), that is, only half of the heterogeneous zone in the second model. This illustrates that the Fresnel zone spreads

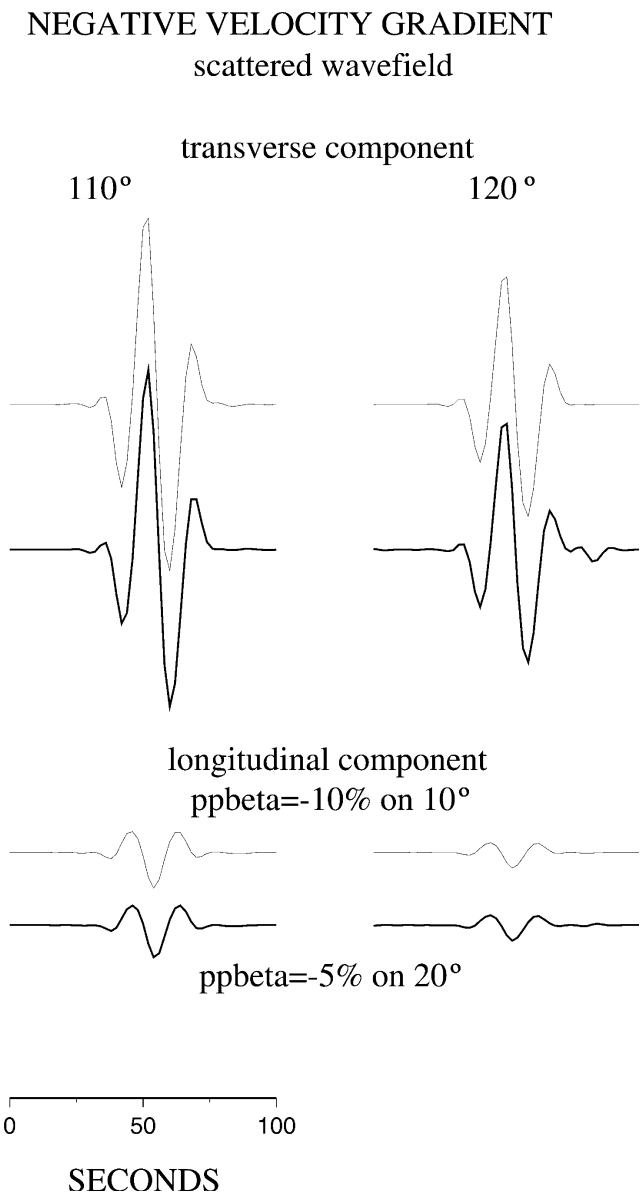

Figure 8. Same as Fig. 7 but with the background model 2 with a negative velocity gradient in D″. Again, the two cases (a and b) shown in Fig. 6 yield almost the same scattered waves, which are stronger and slower than those in Fig. 7.

far beyond this geometrical zone. This shows that a diffracted *S* wave averages nearly linearly perturbations in its Fresnel zone, which can be considerably larger than the geometric diffraction line. The resolution of isolated inhomogeneities located near the great-circle path seems difficult with this wave type.

The next conclusion we can draw from this example is that a very localized (120 km wide) thin ultra-low-velocity zone (-10 per cent) does not modify the amplitude of the direct diffracted *S* wave. Such a thin ultra-low *P*-wave velocity layer has been proposed in order to explain the characteristics of $SP_{\rm diff}KS$ (Garnero & Helmberger 1995, 1996; Helmberger *et al.* 1996) or *PKP* precursors (Vidale & Hedlin 1998; Wen & Helmberger 1998). In this last study, structures with horizontal and vertical length scales of 100–300 and 60–80 km, respectively, and *P*-wave velocity variations of at least 7 per cent were found.

It seems that diffracted *S* waves will be useful in analysing whether these *P*-wave velocity anomalies have an *S*-wave counterpart only if the thickness of the ultra-low-velocity zone is significantly greater than 30 km.

3.3 Variation perpendicular to the great-circle path

In this part, we analyse the variation of the scattered wave amplitude when the heterogeneity is situated out of the great-circle path between the source and the receiver. The inhomogeneity is situated 25 km above the CMB, in a plane crossing the great-circle path at 60° from the source. The distance between the heterogeneity and the great circle varies from 0° to 50° (Fig. 9). Azimuthal variations at the source level are not taken into account in order to keep an identical amplitude for $SV_{\rm inc}$ and $SH_{\rm inc}$ in the different cases and to facilitate comparisons. As expected, we note conversions between $SV_{\rm diff}$ and $SH_{\rm diff}$ when the heterogeneity is not along the great-circle path. In order to analyse better the different waves, the seismograms are shown in the coordinate system related to the heterogeneity–receiver great-circle path. The amplitudes of scattered waves are measured on seismograms convolved with a broad-band instrument response and low-pass filtered. The $SH_{\rm inc}$–$SH_{\rm scat}$ amplitude is always greater by more than a factor of 10 than $SV_{\rm inc}$–$SH_{\rm scat}$. The mechanism producing a scattered *SH* wave from an incident *SV* wave is not very efficient. On the other hand, $SV_{\rm inc}$–$SV_{\rm scat}$ and $SH_{\rm inc}$–$SV_{\rm scat}$ amplitudes are comparable. Since direct $SV_{\rm diff}$ waves are smaller than direct $SH_{\rm diff}$ waves, scattering and coupling are more likely to be observable on the *SV* component. In the following, we will analyse which situation is the most favourable for obtaining large scattered *SV* waves.

We will only consider the case of a unit perturbation of velocity (and $\Delta\rho/\rho = 0$ per cent). The behaviour for $\Delta = 110°$ and 120° is similar. We present here the results at the second distance only. In Fig. 10 it is seen that $SV_{\rm inc}$–$SV_{\rm scat}$ amplitudes decrease gradually when the heterogeneity moves away from the source–receiver great circle (similar behaviour is observed for $SH_{\rm inc}$–$SH_{\rm scat}$). On the other hand, conversion amplitudes increase and reach a maximum for a distance of 30°. In a model with no velocity gradient, the most efficient mechanism to get a scattered *SV* wave is the conversion $SH_{\rm inc}$–$SV_{\rm scat}$ (at latitudes

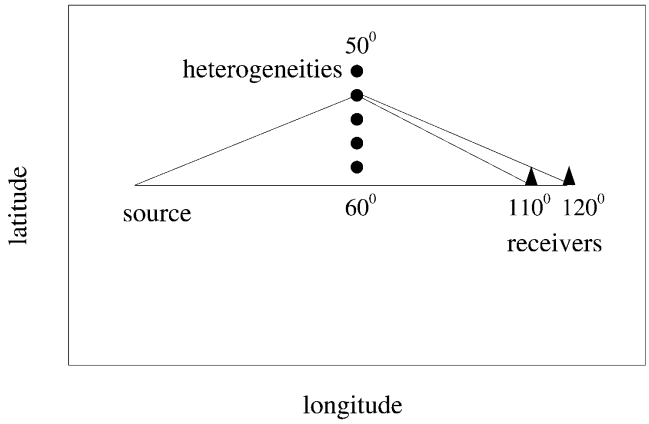

Figure 9. Geometry to study the variation in the perpendicular direction: the inhomogeneities are situated from 0° to 50° away from the great-circle path between the source and the receiver.

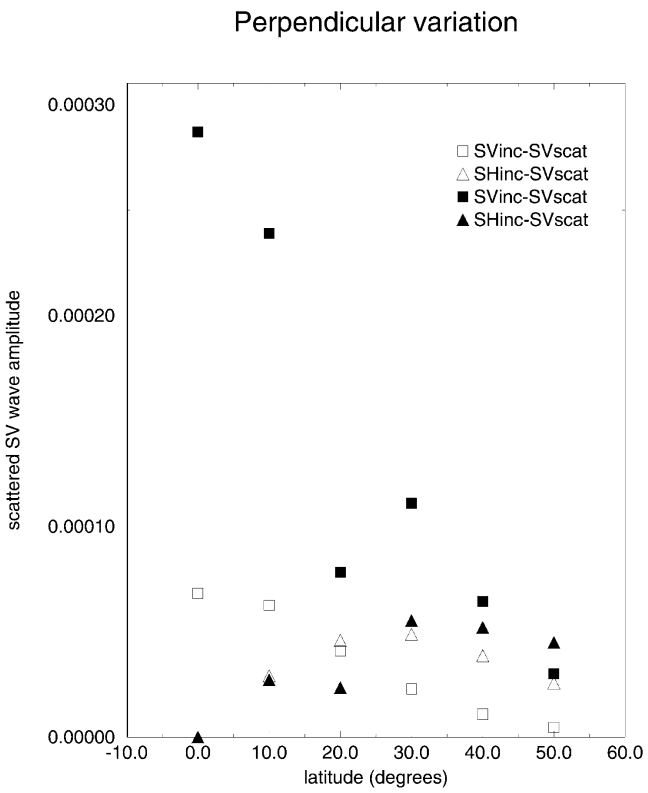

Figure 10. Amplitude variation of a scattered SV wave as a function of the latitude of the heterogeneity for $\Delta = 120°$. $\Delta\beta/\beta = 1$ per cent; longitude of inhomogeneity = 60°; radius = 3505 km; $V_h = 120 \times 120 \times 10$ km^3. At source level $SV_{inc} \sim SH_{inc}$. SH_{inc}–SV_{scat} is often greater than SV_{inc}–SV_{scat} for the background velocity model 1 (open symbols), while the opposite is true for the background velocity model 2 (filled symbols).

larger than 20°). On the other hand, in a model with a negative velocity gradient (filled symbols), the most efficient mechanism remains SV_{inc}–SV_{scat}.

In summary, SV_{inc}–SV_{scat} and SH_{inc}–SV_{scat} have comparable amplitudes and their respective contributions to the total scattered SV wavefield will depend on azimuthal variations at the source level and on the precise geometry of the heterogeneous model. For example, if the inhomogeneity is distributed on both sides of the great-circle path, the conversion terms SH_{inc}–SV_{scat} from both sides of the model will tend to cancel each other (for symmetry reasons), whereas the terms SV_{inc}–SV_{scat} will strengthen.

3.4 Vertical heterogeneity

We analyse whether diffracted S waves can be used to detect very localized vertical inhomogeneities such as mantle plumes. Following the approach for P waves developed by Ji & Nataf (1998a,b), we adopt an extremely simplified plume model by considering a vertical cylinder with constant radius (even though it is probable that mantle plumes widen near the CMB if their source is situated at this level). The cylinder is discretized every 10 km (Fig. 11) and the contributions to the scattered field of the different elements summed together. Moreover, we carry out the calculation only in the D″ layer of 300 km thickness.

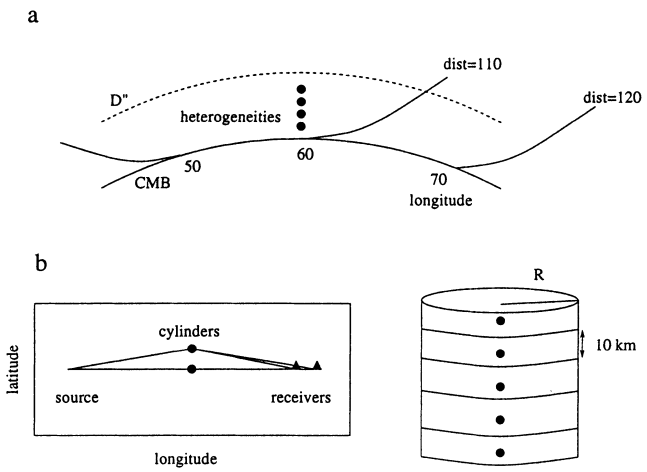

Figure 11. Simplified model of a mantle plume represented by a vertical cylinder. The results presented in Figs 12 and 13 are for a cylinder shifted away from the great-circle path between the source and the receiver. The cylinder is located at 60° longitude, 15° latitude. It has a total height of 300 km and a variable radius R.

If the plume is situated along the great-circle path, we observe no variation in the waveforms or arrival times. The only consequence of the presence of the plume is an increase in amplitude due to focusing. For $\Delta\beta/\beta = -10$ per cent, the amplitude increases by about 15 per cent.

If the cylinder is shifted with respect to the great-circle path between the source and the receiver (Figs 12 and 13), conversions between the two polarizations of diffracted S waves occur and are included in the seismograms. The seismograms are presented in the coordinate system related to the source–station great-circle path. In order to analyse better the conversions, we have taken into account two kinds of sources, the first with no SH amplitude on the great-circle path and the second with no SV amplitude (Table 1). No scattered signal is visible for a cylinder of 60 km radius and a velocity perturbation of –10 per cent. It is necessary to increase the radius to 120 km to see an effect on the seismograms. Recall that the global strength of the heterogeneity depends linearly on $\Delta\beta/\beta$ and on the square of the cylinder radius. Several combinations of ($\Delta\beta/\beta$, R) give the same global strength. We note a complication of the final part of the direct waveforms because scattered waves are late compared to the direct wave. SH_{scat} has a relatively important amplitude in the case with no SH at the source. However, SV_{diff} waves are usually small and difficult to observe at $\Delta = 120°$ on real seismograms. SH_{scat} detection will be pratically impossible. Thus, the most favourable case for detecting scattered waves is that with no SV at the source.

Convection models of mantle plumes designed to explain hotspot volcanism are characterized by pipes with diameters between 100 and 300 km and temperatures excess of 200–600 K. This excess temperature would correspond to a decrease in S velocity between −1 and −2 per cent (Wysession *et al.* 1992). This thermal anomaly would not have any visible effect on seismograms. A chemical anomaly may produce stronger velocity contrasts. Variations for P and S velocity near the CMB as strong as −10 per cent have been proposed recently (Bréger *et al.* 1998; Garnero & Helmberger 1995, 1996; Revenaugh & Meyer 1997; Sylvander *et al.* 1997). 10 per cent perturbation over a sufficiently large volume (cylinder of 120 km radius) can modify the amplitudes of diffracted S waves when the cylinder

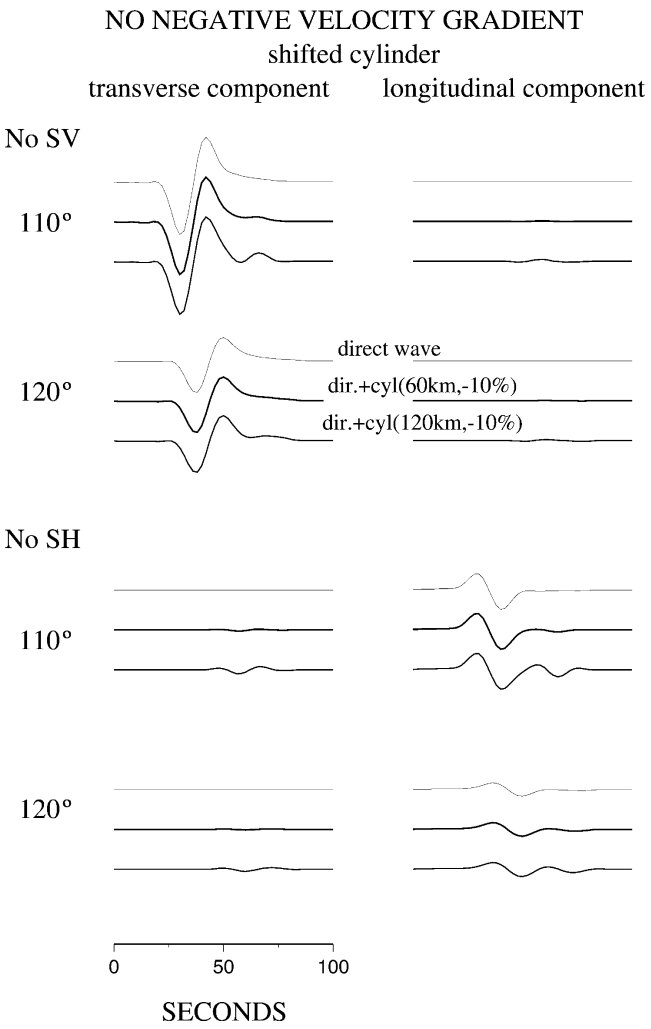

Figure 12. Scattering by a shifted cylinder characterized by its radius and $\Delta\beta/\beta$ perturbation. Synthetic seismograms for longitudinal and transverse components, calculated in a background model with no velocity gradient in D″, convolved with an HRV response and low-pass filtered (origin time $t_0 = 1480$ s for $\Delta = 110°$ and $t_0 = 1559$ s for $\Delta = 120°$). Two kinds of source are used: with no *SV* or no *SH* on the great-circle path (Table 1). Note the complication of the direct waveforms (especially SV_{diff}) and the appearance of converted waves.

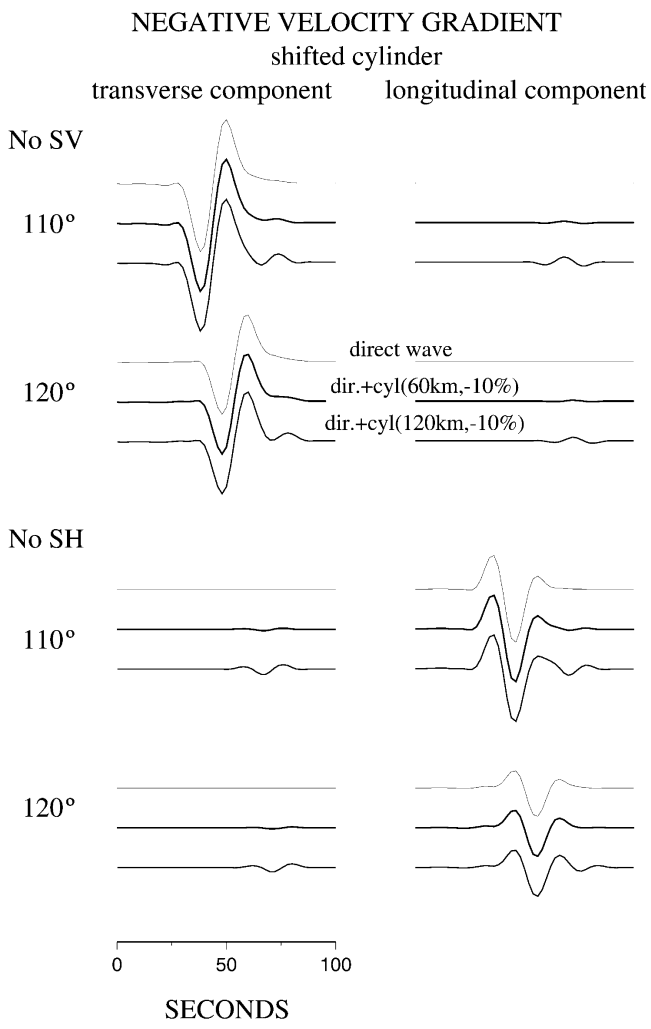

Figure 13. Scattering by a shifted cylinder, background model with a negative velocity gradient. The negative gradient reinforces the direct waves, and the scattered waves look smaller. As SV_{diff} is difficult to observe on real seismograms, the most favourable case to observe scattered waves is the one with no *SV* at the source.

is on the great-circle path between the source and the receiver and modify the waveforms if the cylinder is shifted away. The last case is the most favourable for detecting mantle plumes. As we have shown in the previous part, amplitudes decrease quickly if the heterogeneities are moved further than 30° away from the great-circle path. Consequently, the most favourable conditions for detecting very localized vertical heterogeneities seem to be no *SV* amplitude at the source, a variation of *S* velocity of the order of –10 per cent and a cylindrical volume (240 km diameter, 300 km thickness) that is shifted with respect to the great-circle path between 10° and 30°.

3.5 Random medium

Finally, we analyse the effects on diffracted *S* waves of randomly distributed small-scale heterogeneities in D″. In order to limit multiple interactions between inhomogeneities, we place them in a random way in three planes separated by 100 km (plane radii are 3485, 3585 and 3685 km). The latitudes are between −20° and 20° and the longitudes between 50° and 70°. The minimum distance separating heterogeneities in a plane is 180 km. Each plane contains about 60 inhomogeneities, each with a volume of $60 \times 60 \times 10$ km^3. The velocity contrast is also determined in a random way and is between −10 and 10 per cent. The moment tensor used corresponds to event 860526 (Table 1); the azimuthal variation at the source level is taken into consideration. The seismograms are presented in the source–station coordinate system. We use the model with a negative velocity gradient in D″ as a background model and consider the epicentral distance $\Delta = 110°$. The results are presented in Fig. 14.

The transverse component is more sensitive to the heterogeneities close to the CMB ($r = 3485$ km), whereas the sensitivity of the longitudinal component is maximal 100 km above the CMB. These effects can be explained by the combination of the low-velocity zone, which acts as a waveguide, and the different particle vibrations for SH_{diff} and SV_{diff} near the CMB. Moreover, scattered wave amplitudes are too small

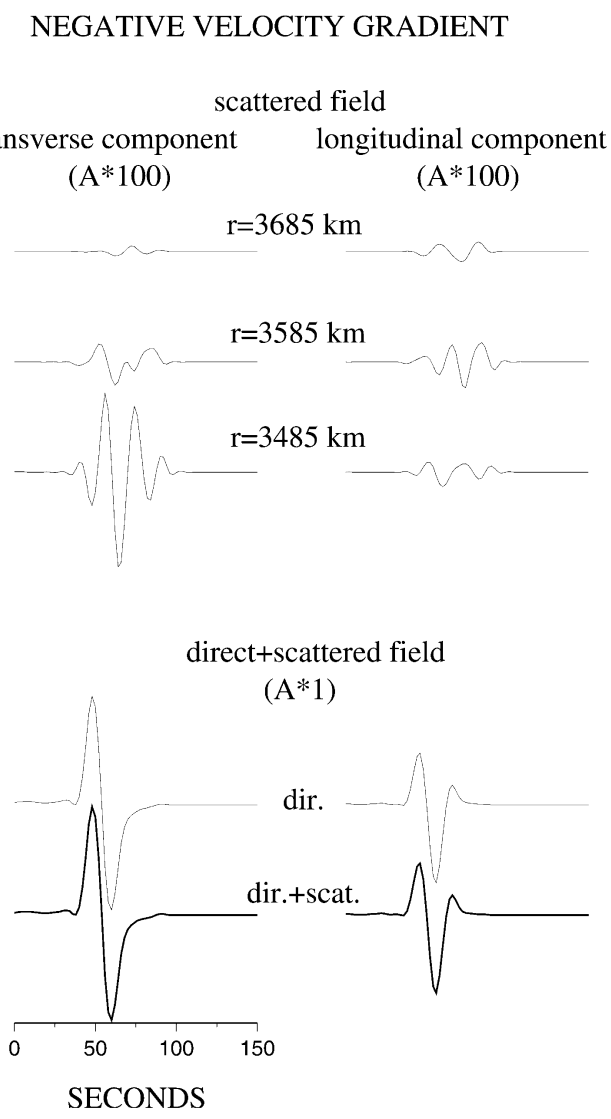

Figure 14. Scattered wavefield obtained for heterogeneities distributed in a random way in three planes of radii 3485, 3585 and 3685 km. Epicentral distance $\Delta = 110^\circ$, background model with a negative velocity gradient in D″, origin time $t_0 = 1470$ s. The transverse component is more sensitive to inhomogeneities close to the CMB. The amplitude of the scattered field is too small to deform the direct waveform.

(by a factor of 100) to modify direct wave amplitudes. Spheres distributed in the D″ layer with 35 km radius and velocity contrasts of the order of 10 per cent for *P* waves can explain short-period (1 Hz) *PKIKP* precursors (Cormier 1995). These waves are extremely favourable for detecting small-scale inhomogeneities near the CMB. On the other hand, such anomalies have negligible effects on S_{diff} waves, which have longer periods (main periods between 10 and 20 s).

4 CONCLUSIONS

In this paper, we have developed a technique to model the propagation of diffracted waves in laterally heterogeneous structures, combining the effects of core diffraction (with the Langer approximation) and scattering by small-scale volumetric inhomogeneities (with the Born approximation). The treatment presented here includes the conversion between the two polarizations of diffracted *S* waves and the coupling between incident and scattered wavenumbers. The method could be extended to an irregular interface or to include the conversions between *S* and *P* waves. It can take into account very localized heterogeneities (Rayleigh scattering) or wider ones by performing a summation on scattering points (Mie scattering). We can describe correctly the effects of heterogeneities located in a broad region characterized by a 300 km thickness above the CMB and 50° width on both sides of the great-circle path between the source and the receiver. Several geophysically interesting geometries have been studied: isolated inhomogeneities, a vertical cylinder, a very localized low-velocity zone, and a random medium. The main advantage of this method is the separation between the direct and the scattered wavefields, as opposed to a method based on finite differences, for example.

Strong variations in amplitudes and waveforms of diffracted *S*-waves are observed on recordings from networks of broadband seismic stations (Emery 1997; Ritsema *et al.* 1997). We have shown that this cannot be explained by weak perturbations of velocity and density, which have a negligible effect on seismograms. It is necessary to reach strong contrasts (of the order of 10 per cent) in sufficiently large volumes to reach observable waveform distortion.

Lateral heterogeneities with such strong contrasts, but in *P*-wave velocity, have been proposed recently by several independent studies. Based on short-period *PKIKP*, Cormier (1995) concluded that random heterogeneities of the order of ± 10 per cent with dimensions of the order of 70 km are present at the base of the mantle. As mentioned earlier, this kind of model does not produce observable effects on diffracted *S* waves, which lack the resolution to detect small-dimension random variations. Heterogeneities of the same order of magnitude, but with larger lateral dimensions, can explain the traveltimes of short-period diffracted *P* waves (Sylvander *et al.* 1997) or long-period waveform distortions (Garnero & Helmberger 1996; Mori & Helmberger 1995). In these models, the low velocity is confined to a relatively thin layer at the base of the D″ layer. It is improbable that ± 10 per cent velocity contrasts can be related to temperature variations alone, and one must invoke chemical anomalies or partial melting. To identify and characterize *S*-wave velocity heterogeneity near the CMB might help to discriminate between different models. As shown here, it seems that the diffracted *S* waves do not have the resolution to detect a 30 km thick layer with an ultra-low *S*-wave velocity. In order to cause observable effects on diffracted *S* waves, the heterogeneities must have relatively large lateral and vertical dimensions.

We found that the most favourable geometry for detecting large anomalies is if they are situated 15°–20° away from the source–station great-circle path. In such situations, the scattered wave arrives in the coda of the direct wave, with a significant coupling between the *SH* and *SV* components. This could be used to plan experiments to detect the base of mantle plumes with array deployment and stacking techniques. We note that the scattered *S* wave may originate equally from the incident *SH* and the incident *SV* waves, and that a scalar treatment (without coupling) would be insufficient. The difference in sensitivity of SV_{diff} and SH_{diff} to the depth of the

heterogeneity could also be exploited: the first samples a thickness of the order of 200 km above the CMB, whereas the second samples a thickness of less than 100 km.

We did not observe any situation where the effect of heterogeneities is similar to the effect of anisotropy, that is, time-delays or coupling between the direct *SH* and *SV* components. Since we model the scattered waves only for periods greater than 4 s, thus having a limited resolution on onset times, and since the waveforms of the different components are quite different, we did not try to measure time delays between different components. However, we did not observe strong delays caused by lateral heterogeneities (for example, the time delay caused by the strong plume model located on the great-circle path is less than 1 s), and they were of the same order of magnitude for the two components. The dominant effect of significant lateral heterogeneity located in the Fresnel zone of the diffracted wave is to modify its amplitude, but the effect on the two components is similar. Of course, our analysis may have some limits due to the Born approximation. We cannot exclude, in some particular geometries, a delay similar to that usually attributed to anisotropy being observed, but we believe that systematic delays observed over a large data set cannot be explained easily by the presence of lateral heterogeneities.

Conversion between the *SH* and *SV* components occurs only when the heterogeneity is significantly out of the source–station epicentral plane. In such cases, the scattered waves arrive in the coda of the direct waves, which are not directly affected by the conversion. Therefore, it also seems that coupling of the *SH* and *SV* direct diffracted waves is more likely to be related to anisotropy than to lateral heterogeneities.

Despite the difficulty of observing SV_{diff} on seismograms for large epicentral distances, a joint study of the two polarizations contains a considerable amount of information on the velocity structure of the D″ layer, including velocity gradient and anisotropy or depth of lateral inhomogeneities. The separation of these effects is difficult. Abnormal S_{diff} waves can be caused by larger volumetric inhomogeneities, low-velocity zones spread out near the CMB or anisotropy.

REFERENCES

Aki, K. & Richards, P.G., 1980a. *Quantitative Seismology: Theory and Methods,* Vol. 1, W. H. Freeman, San Francisco.

Aki, K. & Richards, P.G., 1980b. *Quantitative Seismology: Theory and Methods,* Vol. 2, W. H. Freeman, San Francisco.

Bataille, K. & Lund, F., 1996. Strong scattering of short–period seismic waves by the core–mantle boundary and the P-diffracted wave, *Geophys. Res. Lett.,* **23,** 2413–2416.

Bataille, K., Wu, R.S. & Flatté, S.M., 1990. Inhomogeneities near the core–mantle boundary evidenced from scattered waves: a review, *Pure appl. Geophys.,* **132,** 151–173.

Bréger, L., Romanowicz, B. & Vinnik, L., 1998. Test of tomographic models of D" using differential travel time data, *Geophys. Res. Lett.,* **25,** 5–8.

Chapman, C.H. & Orcutt, J.A., 1985. The computation of body wave synthetic seismograms in laterally homogeneous media, *Rev. Geophys.,* **23,** 105–163.

Chapman, C.H. & Phinney, R.A., 1972. Diffracted seismic signals and their numerical solution, *Methods Comput. Phys.,* **12,** 165–230.

Choy, G.L., 1977. Theoretical seismograms of core phases calculated by frequency-dependent full wave theory, and their interpretation, *Geophys. J. R. astr. Soc.,* **51,** 275–312.

Choy, G.L., Cormier, V.F., Kind, R., Müller, G. & Richards, P.G., 1980. A comparison of synthetic seismograms of core phases generated by the full wave theory and by the reflectivity method, *Geophys. J. R. astr. Soc.,* **61,** 21–39.

Cormier, V.F., 1995. Time-domain modelling of PKIKP precursors for constraints on the heterogeneity in the lowermost mantle, *Geophys. J. Int.,* **121,** 725–736.

Cormier, V.F. & Richards, P.G., 1977. Full wave theory applied to a discontinuous velocity increase: the inner core boundary, *J. Geophys.,* **43,** 3–31.

Cormier, V.F. & Richards, P.G., 1988. Spectral synthesis of body waves in earth models specified by vertically varying layers, in *Seismological Algorithms, Computational Methods and Computer Programs,* pp. 3–45, ed. Doornbos, D.J., Academic Press, London.

Doornbos, D.J., 1976. Characteristics of lower mantle heterogeneities from scattered waves, *Geophys. J. R. astr. Soc.,* **44,** 447–470.

Doornbos, D.J., 1978. On seismic wave scattering by a rough core–mantle boundary, *Geophys. J. R. astr. Soc.,* **53,** 643–662.

Doornbos, D.J., 1981. The effect of a second order velocity discontinuity on elastic waves near their turning point, *Geophys. J. R. astr. Soc.,* **64,** 499–511.

Doornbos, D.J. & Mondt, J.C., 1979a. Attenuation of P and S waves diffracted around the core, *Geophys. J. R. astr. Soc.,* **57,** 353–379.

Doornbos, D.J. & Mondt, J.C., 1979b. P and S waves diffracted around the core and the velocity structure at the base of the mantle, *Geophys. J. R. astr. Soc.,* **57,** 381–395.

Dziewonski, A.M. & Anderson, D.L., 1981. Preliminary reference Earth model (PREM), *Phys. Earth planet. Inter.,* **25,** 297–356.

Emery, V., 1997. Ondes S diffractées à la base du manteau terrestre: modélisation de la diffusion par la structure hétérogène de la couche D", *PhD thesis,* Université de Paris 11.

Fuchs, K., 1968. The reflection of spherical waves from transition zones with arbitrary depth-dependent elastic moduli and density, *J. Phys. Earth,* **16,** 27–41.

Fuchs, K. & Müller, G., 1971. Computation of synthetic seismograms with the reflectivity method and comparison with observation, *Geophys. J. R. astr. Soc.,* **23,** 417–433.

Garnero, E.J. & Helmberger, D.V., 1995. A very slow basal layer underlying large-scale low-velocity anomalies in the lower mantle beneath the Pacific: evidence from core phases, *Phys. Earth planet. Inter.,* **91,** 161–176.

Garnero, E.J. & Helmberger, D.V., 1996. Seismic detection of a thin laterally varying boundary layer at the base of the mantle beneath the central-Pacific, *Geophys. Res. Lett.,* **23,** 977–980.

Garnero, E.J. & Lay, T., 1997. Lateral variations in lowermost mantle shear wave anisotropy beneath the north Pacific and Alaska, *J. geophys. Res.,* **102,** 8121–8135.

Garnero, E.J., Helmberger, D.V. & Engen, G., 1988. Lateral variation near the core–mantle boundary, *Geophys. Res. Lett.,* **15,** 609–612.

Gilbert, F. & Backus, G.E., 1966. Propagator matrices in elastic wave and vibration problems, *Geophysics,* **31,** 326–332.

Haddon, R.A.W. & Cleary, J.R., 1974. Evidence for scattering of seismic PKP waves near the mantle–core boundary, *Phys. Earth planet. Inter.,* **8,** 211–234.

Hedlin, M.A.H., Shearer, P.M. & Earle, P.S., 1997. Seismic evidence for small-scale heterogeneity throughout the Earth's mantle, *Nature,* **387,** 145–150.

Helmberger, D.V., Garnero, E.J. & Ding, X., 1996. Modeling two-dimensional structure at the core–mantle boundary, *J. geophys. Res.,* **101,** 13 963–13 972.

Hock, S., Roth, M. & Müller, G., 1997. Long-period ray parameters of the core diffraction P_{diff} and mantle heterogeneity, *J. geophys. Res.,* **102,** 17 843–17 856.

Hudson, J.A. & Heritage, J.R., 1981. The use of the Born approximation in seismic scattering problems, *Geophys. J. R. astr. Soc.,* **66,** 221–240.

Husebye, E.S., King, D.W. & Haddon, R.A.W., 1976. Precursors to PKIKP and seismic wave scattering near the mantle–core boundary, *J. geophys. Res.,* **81,** 1870–1882.

Ji, Y. & Nataf, H.C., 1998a. Detection of mantle plumes in the lower mantle by diffraction tomography: theory, *Earth planet. Sci. Lett.,* **159,** 87–98.

Ji, Y. & Nataf, H.C., 1998b. Detection of mantle plumes in the lower mantle by diffraction tomography: Hawaii, *Earth planet. Sci. Lett.,* **159,** 99–115.

Kendall, J.M. & Silver, P.G., 1996. Constraints from seismic anisotropy on the nature of the lowermost mantle, *Nature,* **381,** 409–412.

Kennett, B.L.N., 1983. *Seismic Wave Propagation in Stratified Media,* Cambridge University Press, Cambridge.

Kennett, B.L.N. & Illingworth, M.R., 1981. Seismic waves in a stratified half space III—piecewise smooth models, *Geophys. J. R. astr. Soc.,* **66,** 633–675.

Langer, R.E., 1949. The asymptotic solutions of ordinary linear differential equations to the second order, with special reference to a turning point, *Trans. Am. Math. Soc.,* **67,** 461–490.

Lay, T., Williams, Q. & Garnero, E.J., 1998. The core–mantle boundary layer and deep Earth dynamics, *Nature,* **392,** 461–468.

Loper, D.E. & Lay, T., 1995. The core–mantle boundary region, *J. geophys. Res.,* **100,** 6397–6420.

Maupin, V., 1994. On the possibility of anisotropy in the D" layer as inferred from the polarization of diffracted S waves, *Phys. Earth planet. Inter.,* **87,** 1–32.

Mondt, J.C., 1977. Full wave theory and the structure of the lower mantle, *PhD thesis,* University of Utrecht.

Mori, J. & Helmberger, D.V., 1995. Localized boundary layer below the mid-Pacific velocity anomaly identified from a PcP precursor, *J. geophys. Res.,* **100,** 20 359–20 365.

Mula, A.H.G., 1981. Amplitudes of diffracted long-period P and S waves and the velocities and the Q structure at the base of the mantle, *J. geophys. Res.,* **86,** 4999–5011.

Revenaugh, J. & Meyer, R., 1997. Seismic evidence of partial melt within a possibly ubiquitous low-velocity layer at the base of the mantle, *Science,* **277,** 670–673.

Richards, P.G., 1973. Calculations of body–waves, for caustics and tunnelling in core phases, *Geophys. J. R. astr. Soc.,* **35,** 243–264.

Richards, P.G., 1976. On the adequacy of plane-wave reflection/transmission coefficients in the analysis of seismic body waves, *Bull. seism. Soc. Am.,* **66,** 701–717.

Ritsema, J., Garnero, E.J. & Lay, T., 1997. A strongly negative shear velocity gradient and lateral variability in the lowermost mantle beneath the Pacific, *J. geophys. Res,* **102,** 20 395–20 411.

Ritsema, J., Lay, T., Garnero, E.J. & Benz, H., 1998. Seismic anisotropy in the lowermost mantle beneath the Pacific, *Geophys. Res. Lett.,* **25,** 1229–1232.

Snieder, R., 1986a. 3-D linearized scattering of surface waves and a formalism for surface wave holography, *Geophys. J. R. astr. Soc.,* **84,** 581–605.

Snieder, R., 1986b. The influence of topography on the propagation and scattering of surface waves, *Phys. Earth planet. Inter.,* **44,** 226–241.

Snieder, R. & Nolet, G., 1987. Linearized scattering of surface waves on a spherical Earth, *J. Geophys.,* **61,** 55–63.

Souriau, A. & Poupinet, G., 1991. The velocity profile at the base of the liquid core PKP(BC+Cdiff) data: an argument in favour of radial inhomogeneity, *Geophys. Res. Lett.,* **18,** 2023–2026.

Souriau, A. & Poupinet, G., 1994. Lateral variations in P velocity and attenuation in the D" layer, from diffracted P waves, *Phys. Earth planet. Inter.,* **84,** 227–234.

Sylvander, M., Ponce, B. & Souriau, A., 1997. Seismic velocities at the core–mantle boundary inferred from P-waves diffracted around the core, *Phys. Earth planet. Inter.,* **101,** 189–202.

Tarantola, A., 1987. *Inverse Problem Theory: Methods for Data Fitting and Model Parameter Estimation,* Elsevier, Amsterdam.

Tono, Y. & Yomogida, K., 1996. Complex scattering at the core–mantle boundary observed in short-period diffracted P-waves, *J. Phys. Earth,* **44,** 729–744.

Tono, Y. & Yomogida, K., 1997. Origin of short-period signals following P-diffracted waves: a case study of the 1994 Bolivian deep earthquake, *Phys. Earth planet. Inter.,* **103,** 1–16.

Vidale, J.E. & Hedlin, M.A.H., 1998. Evidence for partial melt at the core–mantle boundary north of Tonga from the strong scattering of seismic waves, *Nature,* **391,** 682–685.

Vinnik, L., Farra, V. & Romanowicz, B., 1989. Observational evidence for diffracted SV in the shadow of the Earth's core, *Geophys. Res. Lett.,* **16,** 519–522.

Vinnik, L., Romanowicz, B., Le Stunff, Y. & Makeyeva, L., 1995. Seismic anisotropy in the D" layer, *Geophys. Res. Lett.,* **22,** 1657–1660.

Vinnik, L., Bréger, L. & Romanowicz, B., 1998. On the inversion of Sd particle motion for seismic anisotropy in D", *Geophys. Res. Lett.,* **25,** 679–682.

Weber, M., David, J.P., Thomas, C., Krüger, F., Scherbaum, F., Schlittenhardt, J. & Körnig, M., 1996. The structure of the lowermost mantle as determined from using seismic arrays, in *Seismic Modelling of Earth Structure,* pp. 399–442, eds Boschi, E., Ekström, G. & Morelli, A., Editrice Compositori, Bologne.

Wen, L. & Helmberger, D.V., 1998. Ultra-low velocity zones near the core–mantle boundary from broadband PKP precursors, *Science,* **279,** 1701–1703.

Wu, R. & Aki, K., 1985. Scattering characteristics of elastic waves by an elastic heterogeneity, *Geophysics,* **50,** 582–595.

Wysession, M.E. & Okal, E.A., 1988. Evidence for lateral heterogeneity at the core–mantle boundary from the slowness of diffracted S profiles, in *Structure and Dynamics of Earth's Deep Interior, AGU Monog.,* **46,** 55–63.

Wysession, M.E., Okal, E.A. & Bina, C.R., 1992. The structure of the core–mantle boundary from diffracted waves, *J. geophys. Res.,* **97,** 8749–8764.

APPENDIX A: COUPLING MATRIX

In this Appendix, we detail the elements of the coupling matrix for a point heterogeneity (eqs 67 and 68). The analysis of this matrix has shown that only perturbations in $\Delta\rho$ and $\Delta\mu$ affect the S waves. We recall the general form of each term (eqs 83, 84, 85 and 86) and then take into account the various propagation directions.

A1 Case $SV_{sc}SV_{in}$

A1.1 General expression

$$C_{SV_{sc}SV_{in}} = \frac{-i\omega^2 r_h^2}{2\rho_h\beta_h^3}\, Q^{(2)}[k_{sc}\cos(\theta_r-\theta_h)]\sigma_{sc}V_h$$
$$\times[\Delta\rho n_1(k_{sc}, k_{in}) - 3\Delta\mu n_2(k_{sc}, \eta_{sc}, k_{in}, \eta_{in})$$
$$+ \cos\Psi(\Delta\rho n_3(\eta_{sc}, \eta_{in}) - \Delta\mu n_4(k_{sc}, \eta_{sc}, k_{in}, \eta_{in}))$$
$$- \cos 2\Psi\Delta\mu n_5(k_{sc}, \eta_{sc}, k_{in}, \eta_{in})]\sigma_{in}Q^{(2)}$$
$$\times[k_{in}\cos(\theta_h-\theta_s)]\,. \qquad \text{(A1)}$$

A1.2 $SV_{sc}^{\uparrow}SV_{in}^{\downarrow}$

$\sigma_{sc} = \grave{\sigma}_{sc}$,

$\sigma_{in} = \grave{\sigma}_{in}$,

$$n_1 = \omega^2(\beta p_{sc}/r_h)(\beta p_{in}/r_h)\,, \tag{A2}$$

$$n_2 = (\beta p_{sc}/r_h)(-i\omega\grave{\eta}_{sc})(\beta p_{in}/r_h)(-i\omega\grave{\eta}_{in})\,, \tag{A3}$$

$$n_3 = \omega^2(-\beta\grave{\eta}_{sc})(\beta\grave{\eta}_{in})\,, \tag{A4}$$

$$n_4 = [(-\beta\grave{\eta}_{sc})(-i\omega\grave{\eta}_{sc}) + (\beta p_{sc}/r_h)(-i\omega p_{sc}/r_h)] \times [(\beta\grave{\eta}_{in})(-i\omega\grave{\eta}_{in}) + (\beta p_{in}/r_h)(i\omega p_{in}/r_h)]\,, \tag{A5}$$

$$n_5 = (-i\omega p_{sc}/r_h)(i\omega p_{in}/r_h)(-\beta\grave{\eta}_{sc})(\beta\grave{\eta}_{in})\,. \tag{A6}$$

A1.3 $SV_{sc}^{\uparrow}SV_{in}^{\uparrow}$

$\sigma_{sc} = \grave{\sigma}_{sc}$,

$\sigma_{in} = \acute{\sigma}_{in}$,

$$n_1 = \omega^2(\beta p_{sc}/r_h)(\beta p_{in}/r_h)\,, \tag{A7}$$

$$n_2 = (\beta p_{sc}/r_h)(-i\omega\grave{\eta}_{sc})(\beta p_{in}/r_h)(i\omega\acute{\eta}_{in})\,, \tag{A8}$$

$$n_3 = \omega^2(-\beta\grave{\eta}_{sc})(-\beta\acute{\eta}_{in})\,, \tag{A9}$$

$$n_4 = [(-\beta\grave{\eta}_{sc})(-i\omega\grave{\eta}_{sc}) + (\beta p_{sc}/r_h)(-i\omega p_{sc}/r_h)] \times [(-\beta\acute{\eta}_{in})(i\omega\acute{\eta}_{in}) + (\beta p_{in}/r_h)(i\omega p_{in}/r_h)]\,, \tag{A10}$$

$$n_5 = (-i\omega p_{sc}/r_h)(i\omega p_{in}/r_h)(-\beta\grave{\eta}_{sc})(-\beta\acute{\eta}_{in})\,. \tag{A11}$$

A1.4 $SV_{sc}^{\downarrow}SV_{in}^{\downarrow}$

$\sigma_{sc} = \acute{\sigma}_{sc}$,

$\sigma_{in} = \grave{\sigma}_{in}$,

$$n_1 = \omega^2(-\beta p_{sc}/r_h)(\beta p_{in}/r_h)\,, \tag{A12}$$

$$n_2 = (-\beta p_{sc}/r_h)(i\omega\acute{\eta}_{sc})(\beta p_{in}/r_h)(-i\omega\grave{\eta}_{in})\,, \tag{A13}$$

$$n_3 = \omega^2(-\beta\acute{\eta}_{sc})(\beta\grave{\eta}_{in})\,, \tag{A14}$$

$$n_4 = [(-\beta\acute{\eta}_{sc})(i\omega\acute{\eta}_{sc}) + (-\beta p_{sc}/r_h)(-i\omega p_{sc}/r_h)] \times [(\beta\grave{\eta}_{in})(-i\omega\grave{\eta}_{in}) + (\beta p_{in}/r_h)(i\omega p_{in}/r_h)]\,, \tag{A15}$$

$$n_5 = (-i\omega p_{sc}/r_h)(i\omega p_{in}/r_h)(-\beta\acute{\eta}_{sc})(\beta\grave{\eta}_{in})\,. \tag{A16}$$

A1.5 $SV_{sc}^{\downarrow}SV_{in}^{\uparrow}$

$\sigma_{sc} = \acute{\sigma}_{sc}$,

$\sigma_{in} = \acute{\sigma}_{in}$,

$$n_1 = \omega^2(-\beta p_{sc}/r_h)(\beta p_{in}/r_h)\,, \tag{A17}$$

$$n_2 = (-\beta p_{sc}/r_h)(i\omega\acute{\eta}_{sc})(\beta p_{in}/r_h)(i\omega\acute{\eta}_{in})\,, \tag{A18}$$

$$n_3 = \omega^2(-\beta\acute{\eta}_{sc})(-\beta\acute{\eta}_{in})\,, \tag{A19}$$

$$n_4 = [(-\beta\acute{\eta}_{sc})(i\omega\acute{\eta}_{sc}) + (-\beta p_{sc}/r_h)(-i\omega p_{sc}/r_h)] \times [(-\beta\acute{\eta}_{in})(i\omega\acute{\eta}_{in}) + (\beta p_{in}/r_h)(i\omega p_{in}/r_h)]\,, \tag{A20}$$

$$n_5 = (-i\omega p_{sc}/r_h)(i\omega p_{in}/r_h)(-\beta\acute{\eta}_{sc})(-\beta\acute{\eta}_{in})\,. \tag{A21}$$

A2 Case $SV_{sc}SH_{in}$

A2.1 General expression

$$C_{SV_{sc}SH_{in}} = \frac{-i\omega^2 r_h^2}{2\rho_h\beta_h^3}\,Q^{(2)}[k_{sc}\cos(\theta_r - \theta_h)]\sigma_{sc}V_h \times [\sin\Psi(\Delta\rho n_6(\eta_{sc}) - \Delta\mu n_7(k_{sc}, \eta_{sc}, \eta_{in})) - \sin 2\Psi\Delta\mu n_8(k_{sc}, \eta_{sc}, k_{in})]\sigma_{in}Q^{(2)} \times [k_{in}\cos(\theta_h - \theta_s)]\,. \tag{A22}$$

A2.2 $SV_{sc}^{\uparrow}SH_{in}^{\downarrow}$

$\sigma_{sc} = \grave{\sigma}_{sc}$,

$\sigma_{in} = \grave{\sigma}_{in}$,

$$n_6 = \omega^2(-\beta\grave{\eta}_{sc})(1)\,, \tag{A23}$$

$$n_7 = [(-\beta\grave{\eta}_{sc})(-i\omega\grave{\eta}_{sc}) + (\beta p_{sc}/r_h)(-i\omega p_{sc}/r_h)](-i\omega\grave{\eta}_{in})(1)\,, \tag{A24}$$

$$n_8 = (-i\omega p_{sc}/r_h)(i\omega p_{in}/r_h)(-\beta\grave{\eta}_{sc})(1)\,. \tag{A25}$$

A2.3 $SV_{sc}^{\uparrow}SH_{in}^{\uparrow}$

$\sigma_{sc} = \grave{\sigma}_{sc}$,

$\sigma_{in} = \acute{\sigma}_{in}$,

$$n_6 = \omega^2(-\beta\grave{\eta}_{sc})(1)\,, \tag{A26}$$

$$n_7 = [(-\beta\grave{\eta}_{sc})(-i\omega\grave{\eta}_{sc}) + (\beta p_{sc}/r_h)(-i\omega p_{sc}/r_h)](i\omega\acute{\eta}_{in})(1)\,, \tag{A27}$$

$$n_8 = (-i\omega p_{sc}/r_h)(i\omega p_{in}/r_h)(-\beta\grave{\eta}_{sc})(1)\,. \tag{A28}$$

A2.4 $SV_{sc}^{\downarrow}SH_{in}^{\downarrow}$

$\sigma_{sc} = \acute{\sigma}_{sc}$,

$\sigma_{in} = \grave{\sigma}_{in}$,

$$n_6 = \omega^2(-\beta\acute{\eta}_{sc})(1)\,, \tag{A29}$$

$$n_7 = [(-\beta\acute{\eta}_{sc})(i\omega\acute{\eta}_{sc}) + (-\beta p_{sc}/r_h)(-i\omega p_{sc}/r_h)](-i\omega\grave{\eta}_{in})(1)\,, \tag{A30}$$

$$n_8 = (-i\omega p_{sc}/r_h)(i\omega p_{in}/r_h)(-\beta\acute{\eta}_{sc})(1)\,. \tag{A31}$$

A2.5 $SV_{sc}^{\downarrow}SH_{in}^{\uparrow}$

$\sigma_{sc} = \acute{\sigma}_{sc}$,

$\sigma_{in} = \acute{\sigma}_{in}$,

$$n_6 = \omega^2(-\beta\acute{\eta}_{sc})(1)\,, \tag{A32}$$

$$n_7 = [(-\beta\acute{\eta}_{sc})(i\omega\acute{\eta}_{sc}) + (-\beta p_{sc}/r_h)(-i\omega p_{sc}/r_h)](i\omega\acute{\eta}_{in})(1)\,, \tag{A33}$$

$$n_8 = (-i\omega p_{sc}/r_h)(i\omega p_{in}/r_h)(-\beta\acute{\eta}_{sc})(1)\,. \tag{A34}$$

A3 Case $SH_{sc}SV_{in}$

A3.1 General expression

$$C_{SH_{sc}SV_{in}} = \frac{-i\omega^2 r_h^2}{2\rho_h \beta_h^3}\, Q^{(2)}[k_{sc}\cos(\theta_r - \theta_h)]\sigma_{sc} V_h \times [(-\sin\Psi)(\Delta\rho n_9(\eta_{in}) - \Delta\mu n_{10}(\eta_{sc}, k_{in}, \eta_{in})) - (-\sin 2\Psi)\Delta\mu n_{11}(k_{sc}, k_{in}, \eta_{in})]\sigma_{in} Q^{(2)} \times [k_{in}\cos(\theta_h - \theta_s)]\,. \quad \text{(A35)}$$

A3.2 $SH_{sc}^{\uparrow}SV_{in}^{\downarrow}$

$\sigma_{sc} = \grave{\sigma}_{sc}$,

$\sigma_{in} = \grave{\sigma}_{in}$,

$n_9 = \omega^2(1)(\beta\grave{\eta}_{in})$, (A36)

$n_{10} = (1)(-i\omega\grave{\eta}_{sc})[(\beta p_{in}/r_h)(i\omega p_{in}/r_h) + (\beta\grave{\eta}_{in})(-i\omega\grave{\eta}_{in})]$, (A37)

$n_{11} = (-i\omega p_{sc}/r_h)(i\omega p_{in}/r_h)(1)(\beta\grave{\eta}_{in})$. (A38)

A3.3 $SH_{sc}^{\uparrow}SV_{in}^{\uparrow}$

$\sigma_{sc} = \grave{\sigma}_{sc}$,

$\sigma_{in} = \acute{\sigma}_{in}$,

$n_9 = \omega^2(1)(-\beta\acute{\eta}_{in})$, (A39)

$n_{10} = (1)(-i\omega\grave{\eta}_{sc})[(\beta p_{in}/r_h)(i\omega p_{in}/r_h) + (-\beta\acute{\eta}_{in})(i\omega\acute{\eta}_{in})]$, (A40)

$n_{11} = (-i\omega p_{sc}/r_h)(i\omega p_{in}/r_h)(1)(-\beta\acute{\eta}_{in})$. (A41)

A3.4 $SH_{sc}^{\downarrow}SV_{in}^{\downarrow}$

$\sigma_{sc} = \acute{\sigma}_{sc}$,

$\sigma_{in} = \grave{\sigma}_{in}$,

$n_9 = \omega^2(-1)(\beta\grave{\eta}_{in})$, (A42)

$n_{10} = (-1)(i\omega\acute{\eta}_{sc})[(\beta p_{in}/r_h)(i\omega p_{in}/r_h) + (\beta\grave{\eta}_{in})(-i\omega\grave{\eta}_{in})]$, (A43)

$n_{11} = (-i\omega p_{sc}/r_h)(i\omega p_{in}/r_h)(-1)(\beta\grave{\eta}_{in})$. (A44)

A3.5 $SH_{sc}^{\downarrow}SV_{in}^{\uparrow}$

$\sigma_{sc} = \acute{\sigma}_{sc}$,

$\sigma_{in} = \acute{\sigma}_{in}$,

$n_9 = \omega^2(-1)(-\beta\acute{\eta}_{in})$, (A45)

$n_{10} = (-1)(i\omega\acute{\eta}_{sc})[(\beta p_{in}/r_h)(i\omega p_{in}/r_h) + (-\beta\acute{\eta}_{in})(i\omega\acute{\eta}_{in})]$, (A46)

$n_{11} = (-i\omega p_{sc}/r_h)(i\omega p_{in}/r_h)(-1)(-\beta\acute{\eta}_{in})$. (A47)

A4 Case $SH_{sc}SH_{in}$

A4.1 General expression

$$C_{SH_{sc}SH_{in}} = \frac{-i\omega^2 r_h^2}{2\rho_h \beta_h^3}\, Q^{(2)}[k_{sc}\cos(\theta_r - \theta_h)]\sigma_{sc} V_h \times [\cos\Psi(\Delta\rho n_{12} - \Delta\mu n_{13}(\eta_{sc}, \eta_{in})) - \cos 2\Psi\Delta\mu n_{14}(k_{sc}, k_{in})]\sigma_{in} Q^{(2)}[k_{in}\cos(\theta_h - \theta_s)]\,. \quad \text{(A48)}$$

A4.2 $SH_{sc}^{\uparrow}SH_{in}^{\downarrow}$

$\sigma_{sc} = \grave{\sigma}_{sc}$,

$\sigma_{in} = \grave{\sigma}_{in}$,

$n_{12} = \omega^2(1)(1)$, (A49)

$n_{13} = (-i\omega\grave{\eta}_{sc})(1)(-i\omega\grave{\eta}_{in})(1)$, (A50)

$n_{14} = (-i\omega p_{sc}/r_h)(i\omega p_{in}/r_h)(1)(1)$. (A51)

A4.3 $SH_{sc}^{\uparrow}SH_{in}^{\uparrow}$

$\sigma_{sc} = \grave{\sigma}_{sc}$,

$\sigma_{in} = \acute{\sigma}_{in}$,

$n_{12} = \omega^2(1)(1)$, (A52)

$n_{13} = (-i\omega\grave{\eta}_{sc})(1)(i\omega\acute{\eta}_{in})(1)$, (A53)

$n_{14} = (-i\omega p_{sc}/r_h)(i\omega p_{in}/r_h)(1)(1)$. (A54)

A4.4 $SH_{sc}^{\downarrow}SH_{in}^{\downarrow}$

$\sigma_{sc} = \acute{\sigma}_{sc}$,

$\sigma_{in} = \grave{\sigma}_{in}$,

$n_{12} = \omega^2(-1)(1)$, (A55)

$n_{13} = (i\omega\acute{\eta}_{sc})(-1)(-i\omega\grave{\eta}_{in})(1)$, (A56)

$n_{14} = (-i\omega p_{sc}/r_h)(i\omega p_{in}/r_h)(-1)(1)$. (A57)

A4.5 $SH_{sc}^{\downarrow}SH_{in}^{\uparrow}$

$\sigma_{sc} = \acute{\sigma}_{sc}$,

$\sigma_{in} = \acute{\sigma}_{in}$,

$n_{12} = \omega^2(-1)(1)$, (A58)

$n_{13} = (i\omega\acute{\eta}_{sc})(-1)(i\omega\acute{\eta}_{in})(1)$, (A59)

$n_{14} = (-i\omega p_{sc}/r_h)(i\omega p_{in}/r_h)(-1)(1)$. (A60)